Modeling the Atmospheric Boundary Layer Wind Response to Mesoscale Sea Surface Temperature Perturbations

Citation	Perlin, N., de Szoeke, S. P., Chelton, D. B., Samelson, R. M., Skyllingstad, E. D., & O'Neill, L. W. (2014). Modeling the Atmospheric Boundary Layer Wind Response to Mesoscale Sea Surface Temperature Perturbations. Monthly Weather Review, 142(11), 4284-4307. doi:10.1175/MWR-D-13-00332.1
DOI	10.1175/MWR-D-13-00332.1
Publisher	American Meteorological Society
Version	Version of Record
Terms of Use	http://cdss.library.oregonstate.edu/sa-termsofuse

Modeling the Atmospheric Boundary Layer Wind Response to Mesoscale Sea Surface Temperature Perturbations

NATALIE PERLIN

Rosenstiel School of Marine and Atmospheric Science, University of Miami, Miami, Florida

SIMON P. DE SZOEKE, DUDLEY B. CHELTON, ROGER M. SAMELSON, ERIC D. SKYLLINGSTAD, AND LARRY W. O'NEILL

College of Earth, Ocean, and Atmospheric Sciences, Oregon State University, Corvallis, Oregon

(Manuscript received 25 October 2013, in final form 24 July 2014)

ABSTRACT

The wind speed response to mesoscale SST variability is investigated over the Agulhas Return Current region of the Southern Ocean using the Weather Research and Forecasting (WRF) Model and the U.S. Navy Coupled Ocean–Atmosphere Mesoscale Prediction System (COAMPS) atmospheric model. The SST-induced wind response is assessed from eight simulations with different subgrid-scale vertical mixing parameterizations, validated using Quick Scatterometer (QuikSCAT) winds and satellite-based sea surface temperature (SST) observations on 0.25° grids. The satellite data produce a coupling coefficient of s_U = 0.42 m s^{-1} °C^{-1} for wind to mesoscale SST perturbations. The eight model configurations produce coupling coefficients varying from 0.31 to 0.56 m s^{-1} °C^{-1}. Most closely matching QuikSCAT are a WRF simulation with the Grenier–Bretherton–McCaa (GBM) boundary layer mixing scheme (s_U = 0.40 m s^{-1} °C^{-1}), and a COAMPS simulation with a form of Mellor–Yamada parameterization (s_U = 0.38 m s^{-1} °C^{-1}). Model rankings based on coupling coefficients for wind stress, or for curl and divergence of vector winds and wind stress, are similar to that based on s_U. In all simulations, the atmospheric potential temperature response to local SST variations decreases gradually with height throughout the boundary layer (0–1.5 km). In contrast, the wind speed response to local SST perturbations decreases rapidly with height to near zero at 150–300 m. The simulated wind speed coupling coefficient is found to correlate well with the height-averaged turbulent eddy viscosity coefficient. The details of the vertical structure of the eddy viscosity depend on both the absolute magnitude of local SST perturbations, and the orientation of the surface wind to the SST gradient.

1. Introduction

Positive correlations of local surface wind anomalies with sea surface temperature (SST) anomalies at oceanic mesoscales (10–1000 km) suggest that the ocean influences atmospheric surface winds at these relatively small scales. This is in contrast to the negative correlations found at larger scales in midlatitudes (e.g., Mantua et al. 1997; Xie 2004) that are interpreted as the atmosphere forcing the ocean through wind-driven modulation of surface heat fluxes and ocean mixed layer entrainment (e.g., Frankignoul 1985; Cayan 1992). The mesoscale correlations are based on measurements of surface ocean winds by the SeaWinds scatterometer on board the Quick Scatterometer (QuikSCAT), a microwave radar instrument with a footprint size of ~35 km, and satellite measurements of SST by passive microwave and infrared radiometers (Chelton et al. 2004; Xie 2004; Small et al. 2008).

Motivated by the satellite observations of this ocean–atmosphere interaction, a number of recent modeling studies have addressed the response of the atmospheric boundary layer to mesoscale SST variability (e.g., Small et al. 2008, and references therein). Evaluation of mechanisms for the boundary layer wind response have centered largely on details of the relative roles of the turbulent stress divergence and pressure gradient responses to spatially varying SST forcing. The pressure gradient is driven by the SST-induced variability of

Corresponding author address: Natalie Perlin, Rosenstiel School of Marine and Atmospheric Science, University of Miami, 4600 Rickenbacker Causeway, Miami, FL 33149.
E-mail: nperlin@rsmas.miami.edu

DOI: 10.1175/MWR-D-13-00332.1

planetary boundary layer (PBL) temperature and height, and the overlying free troposphere. There are some differences among previous modeling as to the relative roles of these forcing terms in driving the boundary layer wind response to SST. The primary goal of the present study is to investigate the surface wind response to SST depending on the choice of the PBL mixing scheme. Song et al. (2009) have previously found that the details of the PBL mixing scheme can significantly affect the surface wind response to SST perturbations.

The PBL turbulent mixing parameterizations in numerical models are specifically designed to represent subgrid fluxes of momentum, heat, and moisture through specification of flow-dependent mixing coefficients. Subgrid-scale mixing affects the vertical turbulent stress divergence and pressure gradient, through vertical mixing of temperature and regulation of PBL height and entrainment. PBL parameterizations are especially important near the surface where intense turbulent exchange takes place on scales much smaller than the grid resolution. For estimating the average SST-induced wind changes, Song et al. (2009) and O'Neill et al. (2010b) reported superior performance of a boundary layer scheme based on Grenier and Bretherton (2001, hereafter GB01) that was implemented in a modified local copy of the Weather Research and Forecasting (WRF) Model. The present study extends this model comparison to evaluate the prediction of ocean surface winds by a number of PBL schemes in the WRF atmospheric model, as well as by the U.S. Navy Coupled Ocean–Atmosphere Mesoscale Prediction System (COAMPS) atmospheric model. It includes a new implementation in WRF of the Grenier–Bretherton–McCaa (GBM) PBL scheme (Bretherton et al. 2004), which is an improved version of the GB01 scheme implemented by Song et al. (2009) and O'Neill et al. (2010b). For this comparison, we performed a series of month-long simulations over the Agulhas Return Current (ARC) region in the Southern Ocean, a region characterized by sharp SST gradients and persistent mesoscale ocean meanders and eddies. The simulations are all based on the same SST boundary conditions, specified from a satellite-derived product (Reynolds et al. 2007). This region is far from land, thus avoiding orographic effects that can confuse the interpretation of wind response in coastal regions (e.g., Perlin et al. 2004).

Our general goal is to advance the understanding of the atmospheric response to ocean mesoscale SST variability. Particularly, we evaluate the role of different PBL subgrid-scale turbulent mixing parameterizations, and thereby the dynamics that they represent. First, we assess the near-surface wind response to the small-scale ocean features. We analyze models to identify important mechanisms of PBL momentum and thermal adjustment to the SST boundary condition. We also analyze the vertical extent of the average SST influence on the atmospheric boundary layer wind and thermal structure. We evaluate metrics of eight different PBL parameterizations (six in the WRF Model and two in the COAMPS model), with the objective of identifying how differences between the schemes influence simulations of surface winds.

2. Methods

a. *Numerical atmospheric models and experimental setup*

The WRF Model is a 3D nonhydrostatic mesoscale atmospheric model designed and widely used for both operational forecasting and atmospheric research studies (Skamarock et al. 2005). Version 3.3 of the Advanced Research WRF (hereafter WRF), was used for the present study simulations. The COAMPS atmospheric model is based on a fully compressible form of the nonhydrostatic equations (Hodur 1997), and its version 4.2 was used in the current research study. Of particular importance for this study are the various PBL parameterizations available for these models, which are discussed in section 2b.

Numerical simulations with both models were conducted on two nested domains centered over the ARC in the South Atlantic (Fig. 1). The area features numerous mesoscale ocean eddies and meanders with scales of a few hundred kilometers and associated local SST gradients reaching $1°C\,(100\,km)^{-1}$. This mesoscale structure is superimposed on a large-scale meridional SST gradient in the south Indian Ocean. The model simulation and analysis period is July 2002, which is the same month considered previously in the WRF simulations by Song et al. (2009) and O'Neill et al. (2010b). This winter month in the Southern Hemisphere was characterized by several strong wind events associated with synoptic weather systems that passed through the area. Thus, the effects of mesoscale SST features are investigated here are averaged over a variety of atmospheric conditions. Domain settings are practically identical in WRF and COAMPS. The outer domain has 75-km grid spacing extending 72° longitude by 33° latitude. The nested inner domain has 25-km grid spacing with spatial dimensions of 40° longitude by 17° latitude. The vertical dimension is discretized with a scaled pressure (σ) coordinate grid with 49 layers, progressively stretched from the lowest midlayer at 10 m above the surface up to about 18 km; 22 layers are in the lowest 1000 m.

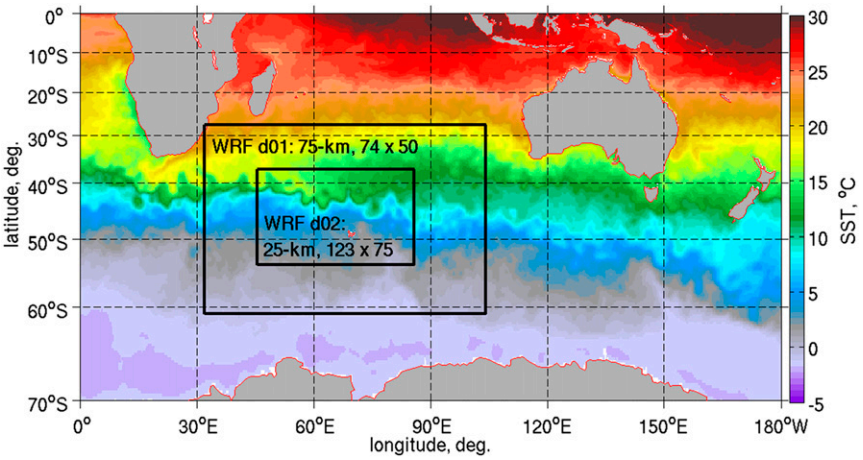

FIG. 1. Monthly average of satellite sea surface temperature (SST, °C) for July 2002 from the NOAA OI 0.25° daily product generated from measurements by the AMSR SST and the AVHRR. Black rectangles outline the WRF outer and nested domains that have 75- and 25-km grid spacing, respectively. Missing OI SST values in the interior of the nested domain that occur as a result of small islands are interpolated for the model lower boundary conditions.

We note that the 25-km grid resolution of our mesoscale atmospheric model simulations is comparable to the grid resolutions of global forecast models. Previous studies have shown that the surface wind response to SST in both the European Centre for Medium-Range Weather Forecasts and the National Centers for Environmental Prediction (NCEP) models is underestimated by nearly a factor of 2 (Chelton and Wentz 2005; Maloney and Chelton 2006; Chelton and Xie 2010). The results of this study therefore have relevance to the accuracy of surface wind fields over the ocean in the global forecast models.

The models were initialized at 0000 UTC 1 July and integrated forward to 0000 UTC 1 August 2002, and were forced at the lateral boundary with the global NCEP Final Analysis (FNL) Operational Global Analysis data on 1.0° × 1.0° grid, available at 6-h intervals. This is the product from the Global Data Assimilation System (GDAS) and NCEP Global Forecast System (GFS) model. Atmospheric boundary conditions on the outer model grid were updated every 6 h.

The SST boundary condition was updated daily in each of the model simulations. We used SST fields from the National Oceanic and Atmospheric Administration (NOAA) version 2 daily optimum interpolation (OI) analyses on a 0.25° grid (Reynolds et al. 2007) as the lower boundary condition for the atmospheric model simulations, and for estimation of the coupling coefficients in conjunction with QuikSCAT winds (see section 3a). Beginning in June 2002, the OI SST analysis combines two types of satellite observations, the Advanced Microwave Scanning Radiometer for Earth Observing System (AMSR-E) and Advanced Very High Resolution Radiometer (AVHRR), and includes a large-scale adjustment of satellite biases with respect to the in situ data from ships and buoys. AMSR-E retrieves SST with a footprint size of about 50 km on a grid spacing of 0.25° with coverage in all but raining conditions (Chelton and Wentz 2005), whereas the AVHRR produces a 4-km gridded product, but only in clear-sky conditions. Missing SST values in the interior of the nested model domain that occur as a result of small islands were interpolated using surrounding values. This minor adjustment of the model's topography to eliminate small islands avoids orographic wind effects in the models, and allows us to isolate the effect of mesoscale SST forcing on the marine boundary layer.

The first day of model output during the spinup was discarded. Model output from the subsequent 30 days was saved at 6-hourly intervals and was used to derive 30-day averages of the variables of interest for the analysis presented in this study. The month-long simulation period and time-averaging statistics were sufficient to obtain a robust statistical relationship between the time-averaged SST and winds. Analysis of the simulations was carried out primarily using the model results from the inner domain.

b. Subgrid-scale parameterizations

1) PBL PARAMETERIZATIONS IN WRF AND COAMPS

PBL schemes (also called boundary layer, turbulence, or vertical mixing schemes) in atmospheric models provide

TABLE 1. List and summary of the eight primary numerical experiments conducted for this study. The name of each experiment combines the name of the atmospheric model (WRF or COAMPS) and name of the boundary layer scheme used. In the WRF v3.3 release, the MYJ PBL scheme had to be used along with the "Eta similarity" surface layer scheme (sf_sfclay_physics = 2). In the WRF_MYJ_SFCLAY case the MYJ PBL was adapted to be used along with the "MM5 similarity" surface scheme (sf_sfclay_physics = 1). See section 2b(2) for other details.

Expt name	PBL-type scheme	PBL scheme reference	Surface flux scheme (sf_sfclay_physics)
WRF_GBM	1.5 order closure	GB01; Bretherton et al. (2004)	MM5 similarity (1)
WRF_MYJ	1.5 order closure	Janjić (1994, 2002)	Eta similarity (2)
WRF_MYJ_SFCLAY	1.5 order closure	Janjić (1994, 2002)	MM5 similarity (1)
WRF_MYNN2	1.5 order closure	Nakanishi and Niino (2006)	MM5 similarity (1)
WRF_UW	1–1.5 order closure*	Brethernon and Park (2009)	MM5 similarity (1)
COAMPS_ipbl = 1	1.5 order closure	Mellor and Yamada (1982); Yamada (1983)	Louis (1979), COARE-2.6 (water)
COAMPS_ipbl = 2	1.5 order closure	Mellor and Yamada (1982); Yamada (1983)	Louis (1979), COARE-2.6 (water)
WRF_YSU	Nonlocal K	Hong et al. (2006)	MM5 similarity (1)

* See notes in section 2b(1) on the WRF UW PBL scheme details.

a means of representing the unresolved, subgrid-scale turbulent fluxes of modeled properties. The eight experiments performed with the various widely used boundary layer parameterization schemes considered here that are available in the WRF and COAMPS models are listed in Table 1: six schemes or their variations were run with the WRF Model, and two schemes were run with the COAMPS model. Experiment names are formed from the model name (WRF or COAMPS), an underscore, and an acronym for the PBL scheme according to the abbreviations given in Table 1.

Turbulent mixing schemes are based on a Reynolds decomposition of the Navier–Stokes equations in which the variables are partitioned into mean and fluctuating components. For example, for property C and vertical velocity w, the mean vertical flux is $\overline{wC} = \overline{w}\,\overline{C} + \overline{w'C'}$, where w' and C' are the fluctuating departures from the respective means $\overline{w}$ and $\overline{C}$. The schemes often parameterize the vertical turbulent flux of any variable $\overline{C}$ as proportional to the local vertical gradient (referred to as the "local-K approach"; Louis 1979), $\overline{C'w'} = -K_C(\partial\overline{C}/\partial z)$, where K_C is a scalar proportionality parameter with units of velocity times distance. A countergradient term is added in some PBL schemes to account for the possibility of turbulent transport by larger-scale eddies that are not dependent on the local gradient.

Four of the WRF experiments and both COAMPS experiments in the present study use PBL parameterizations based on the so-called Mellor–Yamada type 1.5-order turbulence closure, known as level-2–2.5 schemes (Mellor and Yamada 1974, 1982). The term *order closure* refers to the highest order of a statistical moment of the variable for which prognostic equations are solved in a closed system of equations (Stull 1988, chapter 6, see his Table 6-1). In a 1.5-order closure, some but not all the second-moment variables are predicted, and others are parameterized with a diagnostic equation. For most of the 1.5-order schemes considered here, an additional prognostic equation is solved for the turbulent kinetic energy (TKE), defined as $q^2/2$, where $q^2 = u'^2 + v'^2 + w'^2$, but the other second moments (the Reynolds fluxes of the form $\overline{w'C'}$) are parameterized using the local gradient approach, as in a first-order closure. The turbulent eddy transfer coefficients $K_{H,M,q}$ are further parameterized using the predicted q value as follows:

$$K_{M,H,q} = lqS_{M,H,q}, \tag{1}$$

where l is the master turbulent length scale and $S_{M,H,q}$ is a dimensionless stability function. The subscripts M, H, and q in Eq. (1) indicate momentum, heat, and TKE, respectively; and K is the eddy diffusivity for each specific variable. The dimensionless functions $S_{M,H,q}$ in general may depend on stability and wind shear parameters, or may be set to constant values. Here "Mellor–Yamada type" refers to a variety of PBL subgrid-scale mixing schemes developed along the lines of Mellor and Yamada (1974) that parameterize turbulent eddy transfer coefficients in the form of Eq. (1).

Different choices for (or representations of) q, l, and $S_{M,H,q}$ will result in different dependencies of the eddy transfer coefficients on the resolved model state, and different behaviors of the corresponding model boundary layers. A general form of the prognostic equation for the TKE is the following:

$$\frac{D}{Dt}\left(\frac{q^2}{2}\right) - \frac{\partial}{\partial z}\left[K_q\frac{\partial}{\partial z}\left(\frac{q^2}{2}\right)\right] = P_s + P_b - \varepsilon, \tag{2}$$

where D/Dt is the material derivative following the resolved motion; horizontal turbulent diffusion is neglected; P_s and P_b are shear production and buoyant production of turbulent kinetic energy, respectively; and

ε is the dissipation rate. In some schemes, Eq. (2) is replaced, or partly replaced, by an assumption of production-dissipation balance, $(P_s + P_b)/\varepsilon = 1$. For example, the GBM PBL scheme in WRF calculates TKE prognostically using Eq. (2) to obtain q, but assumes production-dissipation balance [after Galperin et al. (1988), their Eqs. (24)–(25)] for the purpose of computing stability functions. This restricts the dependence of $S_{M,H}$ on the wind shear, resulting in a simpler but more robust quasi-equilibrium model.

Our implementation of the GBM PBL scheme in WRF v3.3 follows Song et al. (2009), with some minor code corrections. It is publicly distributed as an option in WRF beginning with version 3.5. The MYJ PBL scheme in WRF v3.3 follows Eqs. (2.5), (2.6), (3.6), and (3.7) in Janjić (2002), employing an analytical solution to determine $S_{M,H}$, with a particular choice of closure constants and dependencies on both static stability and wind shear.

The Mellor–Yamada–Nakanishi–Niino (MYNN) PBL scheme in WRF v3.3 uses a revised set of Mellor and Yamada (1982) closure constants, and is available in the WRF Model as a level-2.5 scheme, and a level-3 scheme (i.e., second-order turbulence closure). For the consistency in comparison with other schemes of similar closure type, only the 2.5-level scheme has been used in our study, which we refer to as MYNN2.

The University of Washington (UW) PBL scheme in WRF v3.3 is a heavily modified version of the GB01 approach that is intended to improve its numerical stability for the use in climate models with longer time steps; it adapts an approach where TKE is diagnosed, rather than being prognosed, which may qualify it as lower than a 1.5-order scheme. The GBM and UW PBL schemes in WRF v3.3 also include an explicit entrainment closure for convective layers that modifies the expression for K_M.

Both COAMPS PBL schemes (set in the COAMPS code by parameters ipbl = 1 and 2) are 1.5-order, level-2.5 schemes that are also based closely on Mellor and Yamada (1982) and Yamada (1983). These schemes use Eqs. (16) and (17) in Yamada (1983) to determine the stability functions based on the flux Richardson number with imposed limits. The COAMPS PBL option ipbl = 2 includes some improvements and code corrections, and is now the recommended option.

The stability function S_q for the TKE diffusivity varies widely between the schemes. Mellor and Yamada (1982) and Janjić (2002) used the constant value $S_q = 0.2$, but the WRF MYJ and COAMPS schemes use the larger constant values $S_q = 5$ and $S_q = 3$, respectively. The GBM and WRF v3.3 MYNN PBL schemes instead set $S_q = 5S_M$ and $S_q = 3S_M$, respectively; the latter differs slightly from the original MYNN $S_q = 2S_M$ from Nakanishi and Niino (2004).

The representations of the turbulent master length scale l, and the boundary layer height if it is included in calculations of the length scale, are different in each of the PBL schemes as well. Additionally, each numerical implementation of the PBL parameterization may contain specific restriction conditions or tuning parameters in order to ensure numerical stability, and may or may not include a countergradient term. It is thus apparent that different PBL schemes based on the same Mellor–Yamada 1.5-order closure approach can perform differently owing to numerous implementation details.

The eighth mixing parameterization considered here, referred to as the Yonsei University (YSU) PBL scheme in WRF v3.3, is not a 1.5-order Mellor–Yamada-type scheme. It is based on Hong and Pan (1996) and Hong et al. (2006), using a nonlocal-K approach (Troen and Mahrt 1986). The scheme diagnoses the PBL height, considers countergradient fluxes, and constrains the vertical diffusion coefficient $K_{M,H}$ to a prescribed profile over the depth of the PBL:

$$K_M = kw_s z\left(1 - \frac{z}{h}\right)^2, \tag{3}$$

where k is the von Kármán constant (0.4), z is the height from the surface, w_s is the mixed-layer velocity scale depending on the friction velocity and the wind profile function evaluated at the top of the mixed layer, and h is the boundary layer height. The eddy diffusivity for temperature and moisture are computed from K_M in Eq. (4) using the Prandtl number. Eddy diffusivity K is calculated locally in the free atmosphere above the boundary layer, based on mixing length, stability functions, and the vertical wind shear. The YSU PBL scheme also includes explicit treatment of entrainment processes at the top of the PBL.

Distinctions between the WRF and COAMPS atmospheric model solutions can also be expected from differences in other physical parameterizations (e.g., convective schemes), numerical discretization schemes, horizontal diffusion schemes, lateral boundary condition, and other factors not related to the choice of the vertical mixing scheme. For example, the differences in vertical discretization in models affect the calculations of vertical gradients, and consequently, the near-surface properties and lower boundary conditions for the TKE equation.

2) SURFACE FLUX SCHEMES

The lower boundary condition for fluxes of momentum, heat, and moisture between the lowest atmosphere

level and the surface are estimated by surface flux schemes. The PBL mixing schemes are sometimes configured and tuned to be run with specific surface flux schemes. A total of three different surface flux schemes were used in the simulations for this study (Table 1). The two surface flux schemes used in the WRF simulations are both based on Monin–Obukhov similarity theory (Monin and Obukhov 1954); they are referred to as ''MM5 similarity'' (sf_sfclay_physics = 1 in Table 1), or ''Eta similarity'' (sf_sfclay_physics = 2). The fifth-generation Pennsylvania State University–National Center for Atmospheric Research (NCAR) Mesoscale Model (MM5) similarity scheme uses stability functions from Paulson (1970), Dyer and Hicks (1970), and Webb (1970) to compute surface exchange coefficients for heat, moisture, and momentum; it considers four stability regimes following Zhang and Anthes (1982), and uses the Charnock relation to relate roughness length to friction velocity over water (Charnock 1955). The Eta similarity scheme is adapted from Janjić (1996, 2002), and includes parameterization of a viscous sublayer over water following Janjić (1994); the Beljaars (1995) correction is applied for unstable conditions and vanishing wind speeds. The COAMPS model uses a bulk scheme for surface fluxes following Louis (1979) and Uno et al. (1995); surface roughness over water follows the Charnock relation; and stability coefficients over water are modified to match the Coupled Ocean–Atmosphere Response Experiment version 2.6 (COARE2.6) algorithm (Fairall et al. 1996; Wang et al. 2002).

To investigate the influence of the differences between the surface flux schemes, we modified the original MYJ PBL scheme in WRF to be used with the same surface flux scheme as the GBM PBL scheme; this simulation was named WRF_MYJ_SFCLAY, and is identical to WRF_MYJ except for the different surface flux scheme.

c. Observations

Satellite observations of vector winds from the microwave scatterometer on board the QuikSCAT satellite on a 0.25° grid in rain-free conditions were used for this study (version 4; Ricciardulli and Wentz 2011). All satellite surface wind measurements over the ocean, including the QuikSCAT winds used here, are calibrated to a reference wind called the equivalent neutral stability (ENS) wind (Ross et al. 1985; Liu and Tang 1996). For consistency with the QuikSCAT data product, the 6-hourly surface winds from the model simulations were converted to model 10-m ENS winds prior to time averaging. The ENS wind is a derived quantity that is defined to be the 10-m wind that would be associated with a given surface stress under reference (neutral) stability conditions. The ENS wind $U_{10m,N}$ considered here is the model 10-m ENS wind, computed as

$$U_{10m,N} = \frac{u_*}{k}\left(\ln\frac{10}{z_0}\right), \tag{4}$$

where the friction velocity u_* and roughness length (in meters) z_0 are taken from each model's surface flux parameterization at each output interval, and $k = 0.4$ is the von Kármán constant. The ENS wind response to mesoscale SST features has been shown from in situ buoy observations to be 10%–30% stronger than the response of the actual 10-m winds (O'Neill 2012). For the ARC region considered here, the difference is about 12% [see Fig. 12 of Song et al. (2009)]. The SST fields used both for the empirical satellite-based estimates of surface wind response to SST (see section 3a) and for the surface boundary condition in each of the model simulations are the NOAA version 2 daily OI SST on a 0.25° grid (Reynolds et al. 2007).

An important distinction between the observed and modeled ENS winds is that QuikSCAT measures the wind relative to the moving sea surface whereas the models are intended to be the absolute winds relative to a fixed coordinate system. Since surface velocity in the ocean is very nearly geostrophic, the magnitude of the surface ocean velocity is approximately proportional to the magnitude of the local SST gradient. Surface currents are, therefore, approximately in quadrature with the SST field. Because of this orthogonality and the generally much smaller magnitudes of surface currents compared with surface wind speeds, the distinction between relative winds and absolute winds has little effect on the coupling coefficient for wind speed that is the primary metric used in this study to assess the SST influence on surface winds (see section 3a).

d. Spatial filtering

A two-dimensional spatial high-pass filter was applied to the observed and modeled fields to separate the mesoscale signal from the larger-scale signal. The filter used here is the quadratic loess smoother developed by Cleveland and Devlin (1988) (see also Schlax and Chelton 1992), which is based on locally weighted quadratic regression. ENS winds or wind stresses and SST were processed using a loess 2-D high-pass filter having an elliptical window with a half-span of 30° longitude × 10° latitude; it is similar to the filter parameters used in Song et al. (2009) study. These filter parameters result in half-power filter cutoffs of 30° longitude × 10° latitude [see Fig. 1 of Chelton and Schlax (2003)]. The high-pass-filtered fields are referred to here as *perturbations*.

To mitigate the edge effects on the loess filter window near the boundaries of the nested grid of the inner domain of the models, the filtering was done over the entire model domain using model output from both the nested and the outer grid. Data from the outer model domain were interpolated onto a 0.25° grid outside of the nested domain. The resulting perturbation fields were analyzed in the region of the nested grid only.

With the spatial high-pass filtering applied to the data, regions of strong SST gradients, and, hence, strong surface ocean currents, correspond to regions of small SST perturbations. As noted in the previous section, the distinction between the relative wind measured by QuikSCAT and the absolute wind simulated by the models consequently has little effect on the wind speed response to mesoscale SST perturbations estimated from the observed and model winds as described in section 3a.

Calculations of the derivative fields, such as ENS wind divergence and vorticity, crosswind and downwind SST gradients, and wind stress curl and divergence, were performed as follows. The instantaneous derivative fields were computed from 6-h output model wind fields. In the case of the QuikSCAT data, the derivative wind fields were computed on a swath-by-swath basis. These instantaneous fields were then averaged over the 30 days and processed using the loess filter with half-span parameters of 12° longitude × 10° latitude. Filtering is less important for the derivative fields since the differentiation is a filter itself, and a smaller filter window could be used. For these derivative variables, the coupling coefficient is not strongly dependent on the precise choice of half-power filter cutoffs for the high-pass filtering (O'Neill et al. 2012).

3. Results

a. Observed coupling coefficients

As the primary metric for estimating air–sea coupling, we adopt the wind speed coupling coefficient s_U, which measures the surface wind speed response to SST perturbations. The coefficient s_U was computed as the slope of a linear regression of bin-averaged 30-day mean ENS 10-m wind perturbations on 30-day mean SST perturbations. The SST perturbations were bin averaged with 0.2°C bin width; mean wind perturbations and their standard deviations were computed for each SST bin.

The wind speed coupling coefficient is simple and has the additional advantage of being relatively invariant to seasonal and geographical variations of the background wind field. The coefficient for wind stress magnitude response to SST perturbations (s_{str}) is also a widely used quantitative estimate of air–sea coupling. Despite the quadratic dependence of wind stress on the wind speed, the wind stress and wind speed coupling coefficients both exhibit approximately linear dependence on the SST perturbations (O'Neill et al. 2012). These coupling coefficients are thus qualitatively similar, but the coupling coefficient for the wind stress magnitude varies seasonally and geographically because it depends on the background wind speed (O'Neill et al. 2012).

The resulting coupling coefficients for the QuikSCAT ENS winds of $s_U = 0.42\,\mathrm{m\,s^{-1}\,°C^{-1}}$, and $s_{str} = 0.022\,\mathrm{N\,m^{-2}\,°C^{-1}}$ for the month of July 2002 (Figs. 2a,b, top right; see Table 3) are very similar to 7-yr estimates for the Agulhas Return Current region obtained by O'Neill et al. (2012) who report values of $0.44\,\mathrm{m\,s^{-1}\,°C^{-1}}$ and $0.022\,\mathrm{N\,m^{-2}\,°C^{-1}}$.

The wind and wind stress responses to mesoscale SST variability modify not only the magnitude of wind and stress, but their directions as well (O'Neill et al. 2010a), which are not reflected in the coupling coefficients for scalar wind speed and wind stress magnitude. Consistent wind direction changes of approximately 10° are observed across midlatitude SST fronts from scatterometer wind fields. Spatial variations in these wind direction perturbations produce surface divergence and curl perturbations that, while pronounced, are surpassed by the contributions from spatial wind speed variations. Satellite observations have previously revealed strong correspondences between wind and wind stress derivative fields and SST derivative fields, and the coupling coefficients for derivative fields have been widely used to assess SST influence on the overlying wind field (Chelton et al. 2001; O'Neill et al. 2005; Chelton et al. 2004, 2007; Haack et al. 2008; Song et al. 2009; Chelton and Xie 2010; O'Neill et al. 2010a; O'Neill et al. 2012). Dynamically, the SST influence on wind stress curl is important because the wind stress curl affects ocean circulation through ocean Ekman layer divergence or convergence. The magnitudes of the curl and divergence of vector winds and wind stress associated with mesoscale SST gradients are found to be comparable to the magnitudes of the basin-scale average curl and divergence (Chelton et al. 2004; O'Neill et al. 2003, 2005; Chelton et al. 2007). The two-way coupling between the ocean mesoscale SST perturbations and atmospheric wind could thus have important effects on upper ocean dynamics and circulation.

For completeness and for comparison with the above-noted previous studies that have assessed ocean–atmosphere coupling on oceanic mesoscales based on derivative wind fields (e.g., Chelton et al. 2004; O'Neill et al. 2010a), we present four additional coupling coefficients that measure the wind and stress responses to

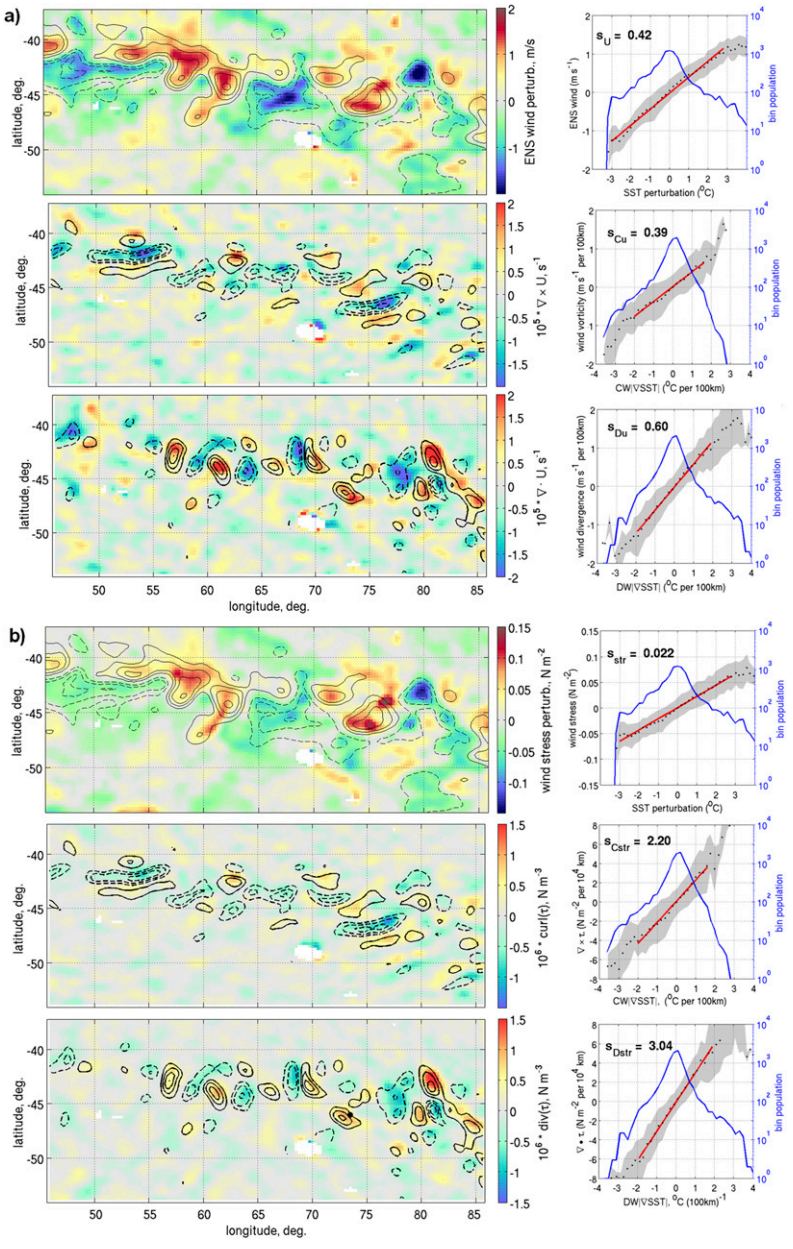

FIG. 2. (a) (top left) July 2002 average of QuikSCAT 10-m ENS wind perturbations (color) and satellite AMSR-E/ Reynolds OI SST perturbations (contours with an interval of 1°C with the zero contour omitted and negative contours shown as dashed lines). (top right) The coupling coefficient s_U estimated as a linear regression slope (red line) of wind perturbations bin averaged on SST perturbations (black dots); the shaded gray areas show ± 1 standard deviation of wind perturbation for each SST bin. Blue lines indicate the number of occurrences within each perturbation SST bin. Estimates include SST perturbations for bins ranging from approximately $-3°$ to $+3°$C that contain >50 data points. (middle row) As in (top row), but for ENS wind curl (vorticity)–crosswind SST gradient perturbation fields; contour intervals of SST gradients are 1°C (100 km)$^{-1}$, with negative contours dashed and the zero contour omitted. The coupling coefficient s_{Cu} is labeled in (right). (bottom row) As in (middle row), but for ENS wind divergence–downwind SST perturbation fields; the coupling coefficient s_{Du} is labeled in (right). (b) (top row) As in (a) (top row), but for QuikSCAT wind stress magnitude–SST perturbation fields with the corresponding coupling coefficient labeled s_{str} in (right). (middle row) As in (a) (middle row), but for the QuikSCAT wind stress–crosswind SST gradient perturbation fields with the coupling coefficient labeled s_{Cstr} in (right). (bottom row) As in (middle row), but for wind stress divergence–downwind SST perturbation fields with the coupling coefficient labeled s_{Dstr} in (right).

SST using spatial derivatives: 10-m ENS wind curl (vorticity) and crosswind SST gradient (s_{Cu}); 10-m ENS wind divergence and downwind SST gradient (s_{Du}); wind stress curl and crosswind SST gradient (s_{Cstr}); wind stress divergence and downwind SST gradient (s_{Dstr}). (The values of these coupling coefficients are shown in Fig. 2 and Table 3.)

As noted in section 2c, QuikSCAT measures the relative wind (the difference between surface vector wind and surface ocean velocity) while the models estimate absolute wind, but this distinction has little effect on the coupling coefficient s_U estimated from QuikSCAT or the models since the surface ocean velocity field is in quadrature with the SST field. For the same reason, the distinction between relative and absolute wind has little effect on the coupling coefficient s_{str} for wind stress magnitude. Moreover, because surface currents in the ocean are very nearly geostrophic and are, therefore, nondivergent, the difference between relative and absolute currents also has little effect on the divergence coupling coefficients s_{Du} and s_{Dstr}.

On the other hand, since surface ocean velocity is approximately proportional and perpendicular to the SST gradient and the SST-induced wind and wind stress curl are both approximately proportional to the crosswind SST gradient, the curl coupling coefficients s_{Cu} and s_{Cstr} are more sensitive to the distinction between relative and absolute winds. Based on geostrophic surface currents estimated from a combination of altimetry (Ducet et al. 2000) and the mean sea surface from the Gravity Recovery and Climate Experiment (GRACE; Rio and Hernandez 2004; Rio et al. 2005), we estimate that the coupling coefficient for the vorticity of absolute winds after taking surface currents into account is roughly 10% larger than the coupling coefficient for the vorticity of relative winds (not shown). The effects of surface currents on the coupling coefficient for the curl of the stress from relative versus surface winds are similar. Since the surface ocean velocity field is not known accurately over the ARC region considered here, it is not possible to adjust the QuikSCAT winds to obtain absolute winds for comparison with the model winds. It must, therefore, be kept in mind that comparisons between the curl coupling coefficients estimated from QuikSCAT winds and the model winds are affected to some degree by surface ocean currents. This issue could be resolved by running the mesoscale atmospheric models in a fully coupled configuration, which would enable the calculation of relative winds from the models that would be directly comparable to the winds measured by QuikSCAT. Coupled simulations are beyond the scope of the present study. Figures 2a and 2b demonstrate high visible correspondence between spatially high-pass-filtered fields of monthly average quantities of observed wind/wind stress derivatives and SST derivatives (left columns). The approximately linear relationships between the wind response in different SST bins justify the use of the coupling coefficient obtained by linear regression as the primary metric considered here for model representation of SST influence on surface winds (right columns, see the figure caption for details).

b. *Model surface winds and coupling coefficients*

1) MEAN WINDS

The study period of July 2002 was characterized by strong austral winter westerly winds and several strong synoptic weather systems propagating eastward through the area. The monthly averages of ENS 10-m winds (Fig. 3, shaded) indicate broad similarity between models and observations, but with some notable differences. Particular simulations vary in wind strength and in details of spatial structure of the average wind fields. The three WRF simulations using different Mellor–Yamada-type schemes (GBM, MYNN2, and UW) and the WRF_YSU scheme (refer to Table 1) simulate the stronger wind in the eastern part of the domain, in agreement with QuikSCAT. The other four simulations all underestimate the winds and show less spatial variability. The strongest wind in the domain is found in the east rather than aligned with the strongest meridional gradient of SST along 42°S in Fig. 1. We will later assess spatial variability of the surface winds in response to underlying mesoscale SST changes.

2) SPATIAL SCALES OF VARIABILITY

Zonal power spectral density (PSD) estimates of mean July 2002 SST perturbations and wind perturbations (Fig. 4) show a small peak in both variables at wavelengths near 300 km (in the middle of the oceanic mesoscale band). The broad peak at wavelength scales of about 1000 km (close to the synoptic scale) arises from attenuation of power at longer scales by the spatial high-pass filtering applied to the wind and SST fields (see section 2d). The WRF_GBM simulation is in better agreement with QuikSCAT in the synoptic-to-mesoscale range (i.e., for wavelengths of ~200 km and greater). The COAMPS simulation with ipbl = 2 underestimates the PSD at wavelengths between 500 and 1000 km. Other models tend either to overestimate or underestimate the PSD at all scales, except for WRF_YSU, which is close to the QuikSCAT estimates at about 400-km wavelength. With the major spectral peak found near 300 km for both wind and SST perturbations, the model resolution of the nested domain with

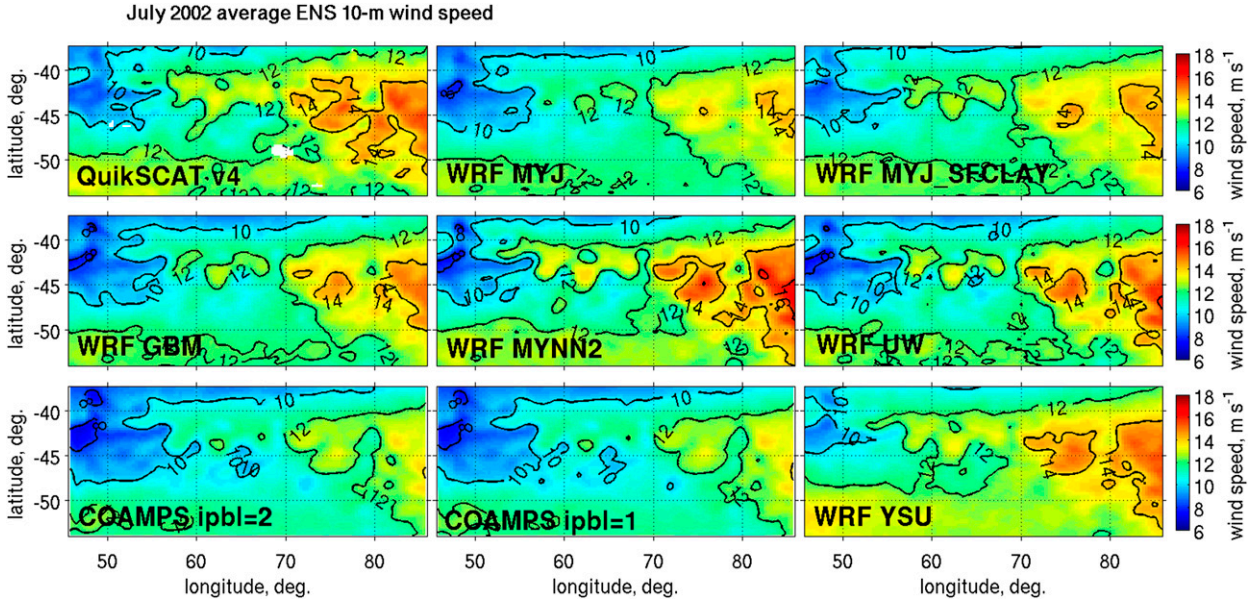

FIG. 3. The July 2002 mean 10-m equivalent neutral stability (ENS) wind speeds ($m\,s^{-1}$), over the model nested domain area, from QuikSCAT v4 observations and the eight model simulations as indicated in the bottom-left corner of each panel. QuikSCAT winds included 1.25° ×1.25° smoothing with a loess filter.

25-km grid boxes appears to be adequate enough to capture the important features.

3) WIND SPEED–SST COUPLING COEFFICIENTS

As in all previous studies, the mesoscale variability of the average ENS 10-m wind speed and SST fields (Fig. 5) indicates that warm SST perturbations are consistently aligned with perturbations of stronger wind speed. Wind speed is thus higher over warmer water and lower over colder water. Visual inspection of the amplitudes of the maximum and minimum wind speed perturbations reveals that WRF_MYNN2 and WRF_UW both overestimate the amplitudes while WRF_MYJ underestimates them. WRF_GBM visually agrees best with QuikSCAT, with COAMPS_ipbl = 2 only slightly smaller in amplitude.

Comparison of the coupling coefficients obtained by linear regression of the time-mean ENS wind speed and SST perturbations for QuikSCAT and the models (Fig. 6) confirms the visual impressions summarized above: WRF_GBM produced $s_U = 0.40\,m\,s^{-1}\,°C^{-1}$, the value closest to the QuikSCAT estimate ($0.42\,m\,s^{-1}\,°C^{-1}$), followed by COAMPS ipbl = 2, COAMPS_ipbl = 1, and WRF_YSU (0.38, 0.36, and $0.35\,m\,s^{-1}\,°C^{-1}$, respectively). Excessively large s_U resulted for WRF_MYNN2 and WRF_UW (0.56 and $0.53\,m\,s^{-1}\,°C^{-1}$, respectively), and the weakest $s_U = 0.31\,m\,s^{-1}\,°C^{-1}$ resulted for WRF_MYJ.

To test whether differences between the experiments could be attributable to the different surface flux scheme, we replaced the "Eta similarity" surface scheme in WRF_MYJ with the "MM5 similarity" surface flux scheme that is similar to what is used in WRF_GBM and other models (refer to Table 1). The simulation with this modification, referred to as WRF_MYJ_SFCLAY, slightly increased the s_U from 0.31 to $0.34\,m\,s^{-1}\,°C^{-1}$,

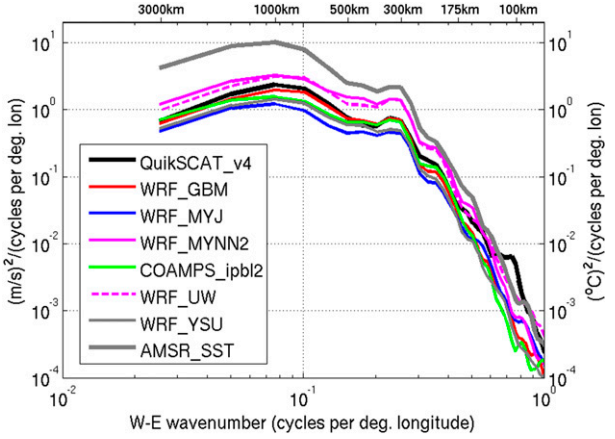

FIG. 4. Power spectral densities computed for the nested domain area from the spatially high-pass-filtered monthly mean SST (the thick gray line, with scale defined by the right *y* axis), and ENS 10-m winds (with scale defined by the left *y* axis). Spectral density estimates were computed for individual latitudinal bands within the nested domain and then averaged. Results from six out of eight model simulations listed in Table 1 are shown. Results from the simulations WRF_MYJ_SFCLAY and COAMPS_ipbl1 were relatively similar to WRF_MYJ and COAMPS_ipbl2, correspondingly, and were omitted to avoid clutter.

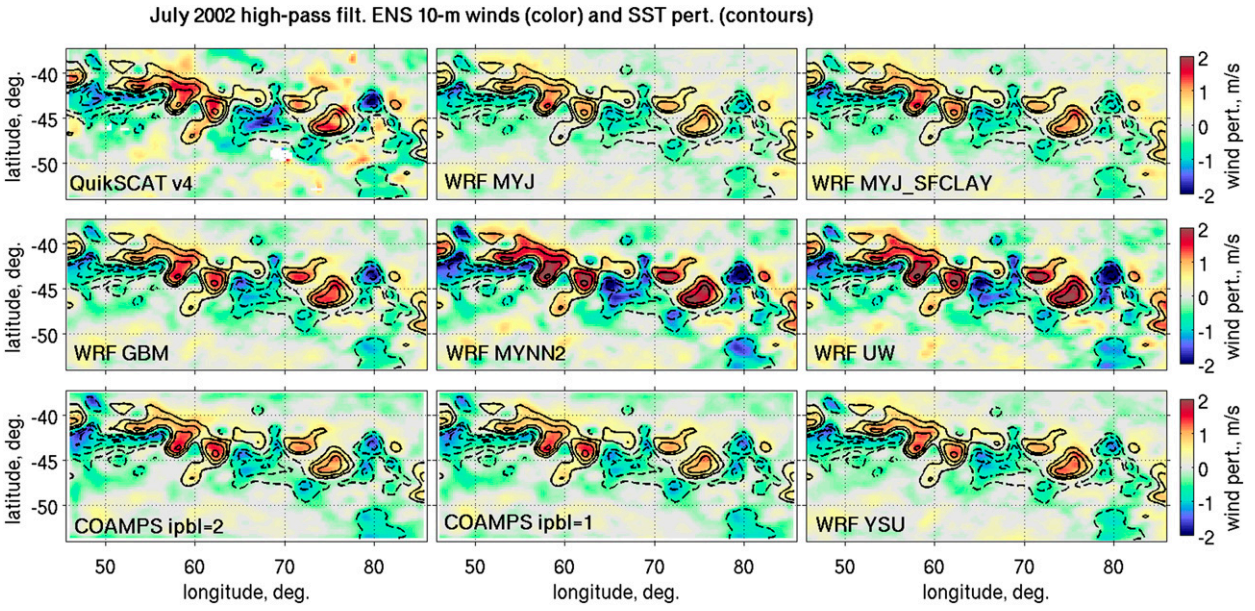

FIG. 5. The July 2002 averages of 10-m ENS wind perturbations (color), and Reynolds OI SST perturbations (contours), similar to the top-left panel of Fig. 2a. Wind speed perturbations are shown from the (top left) QuikSCAT satellite wind product (v4) with 1.25° × 1.25° smoothing with a loess filter; (other panels) the eight model simulations (WRF v3.3 or COAMPS) as indicated, with various turbulent mixing schemes.

which is still almost 20% smaller than the QuikSCAT estimate. Wind stress and surface flux differences from the WRF_MYJ_SFCLAY simulation (not shown) indicate that the MM5 similarity surface scheme was more sensitive to the local SST changes, consistent with higher coupling coefficient found for WRF_MYJ_SFCLAY.

An additional test was performed for the WRF_UW simulation by including the Zhang–McFarlane cumulus parameterization (cu_physics = 7; Zhang and McFarlane 1995) and the shallow convection scheme (shcu_physics = 2; Bretherton and Park 2009), both adapted from the Community Atmosphere Model

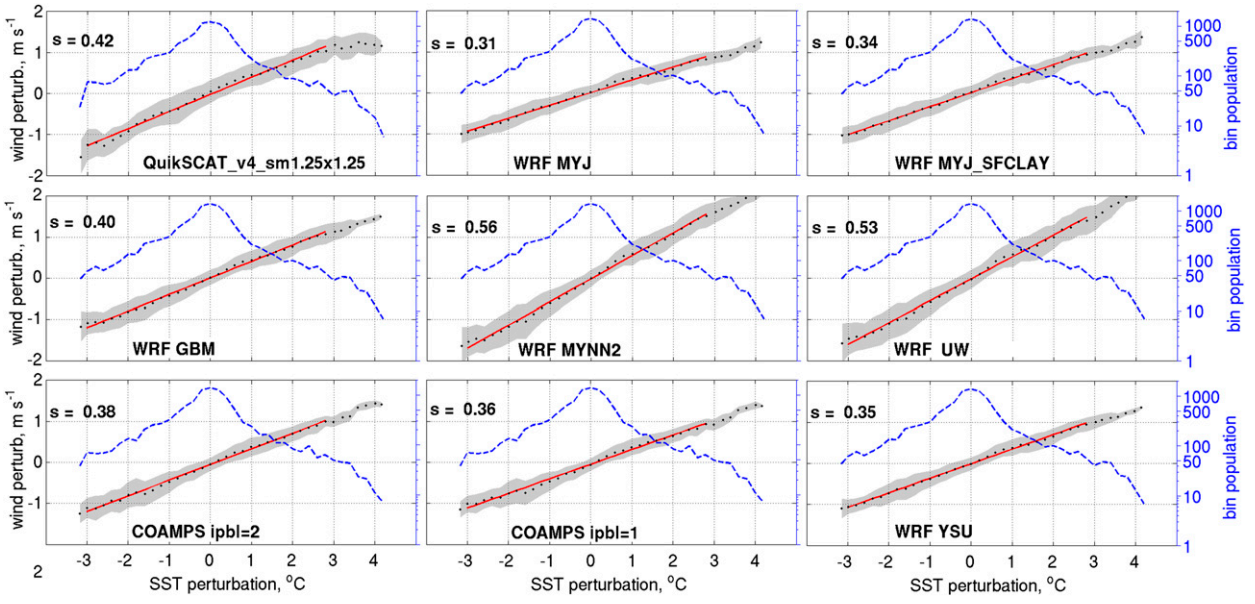

FIG. 6. Coupling coefficients s_U (labeled as "s" in each panel) between the ENS 10-m wind speed and SST perturbation fields shown in Fig. 5, as in the top-right panel of Fig. 2a.

(CAM), as was the UW_PBL mixing scheme itself. While inclusion of these physical options has been shown to work well together in CAM (R. J. Small 2013, personal communication), they resulted in only a slight reduction of $s_U = 0.51\,\mathrm{m\,s^{-1}\,°C^{-1}}$ compared to 0.53 in WRF without the cumulus parameterization and shallow convection scheme.

We also tested one additional vertical mixing scheme that is available in WRF v3.3, the nonlocal-K profile GFS PBL scheme (Hong and Pan 1996) that is a predecessor of the YSU PBL scheme (Hong et al. 2006), over which the YSU PBL has been shown to be a notable improvement. GFS PBL yielded a coupling coefficient of only $s_U = 0.23\,\mathrm{m\,s^{-1}\,°C^{-1}}$. Because it produced the weakest coupling coefficient among all of the experiments, the GFS PBL scheme was not considered for further analysis. Weakness of the GFS PBL performance and limitations of the YSU PBL schemes are likely due to these schemes' constraint of the eddy viscosity and diffusivity profiles to a specific shape within the boundary layer. The importance of the vertical profiles of eddy mixing coefficients for surface wind prediction is discussed in the text in section 3c(2).

4) Relation of the large-scale wind to mesoscale wind speed–SST coupling

Because of the significant differences among the mean wind speed fields from the eight model simulations and among their mesoscale wind–SST coupling coefficients, we investigated the possibility that the mesoscale statistics were influenced by differences in the large-scale background winds. We found that strong domain-mean ENS 10-m winds in the simulations do not imply strong mesoscale wind variability. For example, both COAMPS simulations produced reasonable coupling coefficients (Fig. 6), but underestimated the mean wind speed (Fig. 3).

In an attempt to separate the large-scale and mesoscale contributions to the total wind in the models, the total 30-day average wind speed and SST fields (U, T) were partitioned into spatial means over the entire domain (and) and two spatially variable components, large-scale variations ($\langle U\rangle$ and $\langle T\rangle$), and mesoscale perturbations (U' and T'), where the last two are defined by the half-power filter cutoffs of the two-dimensional loess smoother. The spatial covariance of the time-mean speed and SST, cov(U, T), can then be written as

$$\begin{aligned}\mathrm{cov}(U,T) &= \overline{(U-\overline{U})(T-\overline{T})}\\ &= \overline{(\langle U\rangle + U' - \overline{U})(\langle T\rangle + T' - \overline{T})}. \qquad (5)\end{aligned}$$

After carrying out the multiplication in the above equation, rearranging the resulting nine terms, and noting that small-scale averages ($\overline{U'}$, $\overline{T'}$) over the entire domain are numerically negligible, the covariance in Eq. (5) is closely approximated by four individual components as follows:

$$\begin{aligned}\mathrm{cov}(U,T) \approx\ & \underbrace{\mathrm{cov}(\langle U\rangle,\langle T\rangle)}_{\mathrm{I}} + \underbrace{\mathrm{cov}(\langle U\rangle,T')}_{\mathrm{II}}\\ & + \underbrace{\mathrm{cov}(U',\langle T\rangle)}_{\mathrm{III}} + \underbrace{\mathrm{cov}(U',T')}_{\mathrm{IV}}. \qquad (6)\end{aligned}$$

The left-hand side of Eq. (6) is the spatial covariability of the temporal mean quantities. Term I on the right-hand side (rhs) is the covariance of large-scale (low-pass filtered) U and T fields. The cross terms II and III evaluate the covariability of a large-scale of one variable with the mesoscale of the other variable. Term IV represents the mesoscale covariability of the wind and SST that is proportional to the regression slope s_U. This decomposition of covariance into four components places the mesoscale covariability into the context of the total and large-scale covariability. The covariances and variances (σ^2) of the different pairs of U and T variables in Eq. (6) are listed in Table 2, and the correlation coefficients for the corresponding terms are shown in Fig. 7.

The large-scale wind speed and SST fields (term I) are negatively correlated (Table 2 and the light blue bars in Fig. 7). Since the mesoscale perturbations are small relative to the large-scale wind speeds, the time-averaged wind speed and SST fields [the lhs of Eq. (6)] are also negatively correlated (Table 2 and the dark blue bars in Fig. 7). This result agrees with previous observations of negative correlations between wind speed and SST on large scales (e.g., Xie 2004), consistent with increased evaporative cooling of the ocean by surface winds.

All the terms on the rhs of Eq. (6) involving perturbation fields have positive covariances (data columns 3–5 in Table 2 and the green, orange and red bars in Fig. 7). The positive correlation between $\langle U\rangle$ and T' in term II, representing stronger larger-scale wind speeds at the locations of the positive small-scale SST perturbations, is very small. The correlation between mesoscale wind perturbations U' and the large-scale SST $\langle T\rangle$ in term III is also positive in all of the models with slightly larger magnitude. The positive correlations of the mesoscale perturbations U' and T' are by far the strongest (Fig. 7). These mesoscale perturbations and their covariability are the focus of the present study.

5) What determines the coupling coefficient?

The coupling coefficient s_U, obtained by linear regression on the binned averages as described in section 3a can be expressed in terms of the correlation $\rho_{U'T'}$ as follows:

TABLE 2. Covariances and variances (σ^2) of the time average, large-scale (spatially low-pass filtered), and mesoscale (spatially high-pass filtered) SST and ENS winds from QuikSCAT and the eight models simulations. Units for the covariances are °C m s^{-1}; units for the variances of wind variables are m^2 s^{-2}. Variances of SST are essentially the same for all of the simulations because of the same SST boundary condition was used for every model, differing as follows because of the different model interpolation procedures: Variances of NOAA SST are $\sigma^2(T) = 23.27(°C)^2$, $\sigma^2(\langle T\rangle) = 20.49(°C)^2$, and $\sigma^2(T') = 1.27(°C)^2$. Variances for WRF SST are $\sigma^2(T) = 23.79(°C)^2$, $\sigma^2(\langle T\rangle) = 20.30(°C)^2$, and $\sigma^2(T') = 1.27(°C)^2$. Variances for COAMPS SST are $\sigma^2(T) = 23.14(°C)^2$, $\sigma^2(\langle T\rangle) = 20.56(°C)^2$, and $\sigma^2(T') = 1.23(°C)^2$.

Database	cov(U, T)	cov($\langle U\rangle$, $\langle T\rangle$)	cov($\langle U\rangle$, T')	cov(U', $\langle T\rangle$)	cov(U', T')	$\sigma^2(U)$	$\sigma^2(\langle U\rangle)$	$\sigma^2(U')$
QuikSCAT v4	−0.63	−1.49	0.03	0.31	0.52	1.92	1.55	0.30
WRF_GBM	−1.58	−2.39	0.05	0.26	0.49	2.02	1.66	0.25
WRF_MYJ	−1.41	−2.13	0.06	0.28	0.28	1.54	1.26	0.15
WRF_MYJ_SFCLAY	−0.90	−1.67	0.07	0.29	0.41	1.41	1.10	0.18
WRF_MYNN2	−1.06	−2.14	0.07	0.32	0.69	2.47	1.88	0.46
WRF_UW	−1.28	−2.32	0.05	0.33	0.66	2.22	1.72	0.43
WRF_YSU	−1.41	−2.16	0.05	0.27	0.43	1.57	1.29	0.19
COAMPS_ipbl = 1	−1.01	−1.82	0.06	0.30	0.45	1.42	1.15	0.21
COAMPS_ipbl = 2	−1.00	−1.81	0.06	0.28	0.48	1.47	1.15	0.23

$$s_U = \rho_{U'T'}\frac{\sigma_{U'}}{\sigma_{T'}}, \tag{7}$$

where $\sigma_{U'}$, $\sigma_{T'}$ are the corresponding standard deviations of the wind and SST perturbation fields, respectively, estimated from the fields shown in Fig. 5. As noted in the previous section, the correlation coefficients $\rho_{U'T'}$ are generally high for all of the models, falling within the narrow range of 0.86–0.92, as shown in Fig. 7. The standard deviation of temperature $\sigma_{T'} = 1.1$°C is nearly identical for all of the models as it is prescribed by the imposed surface forcing. Differences between the values of the coupling coefficients s_U are thus primarily determined by the standard deviation of the model wind speed perturbations $\sigma_{U'}$. Indeed, Fig. 8b shows that the correlation between wind perturbation variance $\sigma^2_{U'}$ and s_U is 0.996 among the eight model simulations. In contrast, no statistically significant correlations are found between the domain-averaged wind speed and s_U (Fig. 8a). Spatial variances of time-mean total wind speed U and mesoscale wind speed perturbations U' over the nested domain are found to be highly correlated at $\rho = 0.94$ (Fig. 8c). The process of mesoscale wind response to SST is thus the primary contribution to the total spatial variability of the wind field.

6) COUPLING COEFFICIENTS FOR OTHER WIND VARIABLES

To facilitate comparisons with earlier estimates of mesoscale air–sea coupling, we present several other metrics in the form of coupling coefficients for wind stress magnitude, and derivatives of vector winds and wind stress (i.e., the curl and divergence). For these, wind stress magnitude is regressed onto SST, while wind stress curl and divergence are regressed onto the crosswind and downwind SST gradient components, respectively (see Chelton et al. 2004; O'Neill et al. 2010a). The rationale for use of the derivative fields for assessing the model representations of SST influence on the surface wind field were discussed in section 3a. Table 3 shows a summary of the six different coupling coefficients, and the

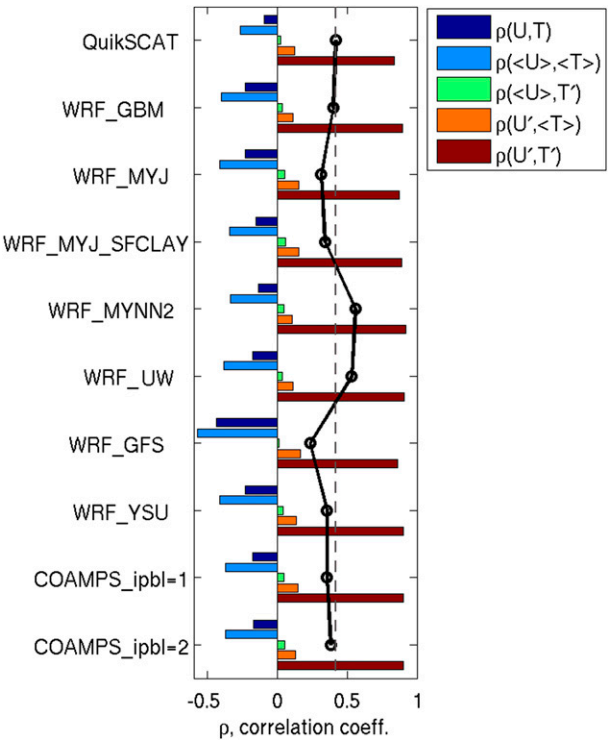

FIG. 7. Correlations between the pairs of mean 10-m ENS winds and SST fields, and their spatially low-pass and high-pass components, from Eq. (7). Black open circles indicate the coupling coefficients s_U for QuikSCAT and the eight experiments according to the numerical values on the x axis, but in m s^{-1} °C^{-1}. Dashed line passes through the value of the QuikSCAT coupling coefficient.

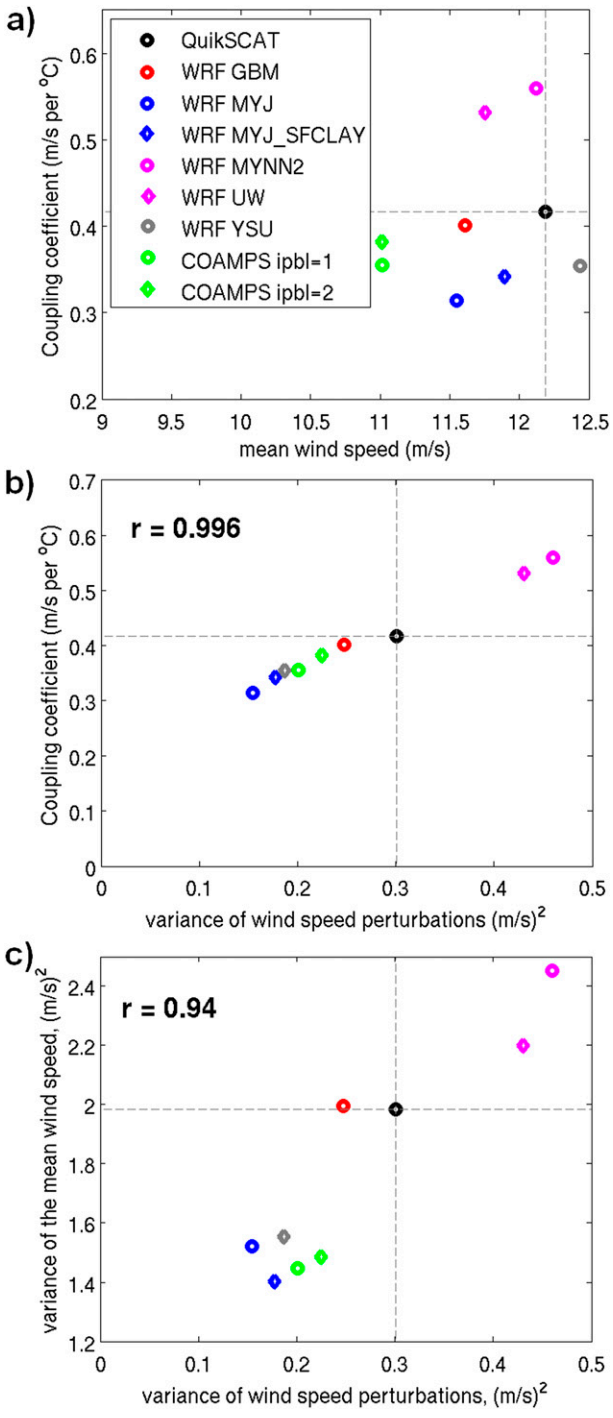

FIG. 8. Mean statistics over the nested domain for QuikSCAT and the eight model simulations: (a) wind speed coupling coefficients vs the corresponding mean ENS 10-m winds; (b) wind speed coupling coefficients vs spatial variance of ENS wind speed perturbations $\sigma^2_{U'}$, with the label "r" corresponding to the correlation coefficient computed over the nine points; and (c) spatial variance of the time-averaged ENS wind σ^2_U vs spatial variance of ENS wind perturbations $\sigma^2_{U'}$ (i.e., variance of the fields shown in Fig. 3 vs the corresponding fields from Fig. 5), with the label "r" corresponding to the correlation coefficient between the nine points. The black dashed lines pass through the QuikSCAT estimate in each panel.

ratio of each to its corresponding estimate from QuikSCAT wind fields. The mean and standard deviation of these ratios for each of the eight experiments (in the order of Table 3) are: 0.81 ± 0.10, 0.89 ± 0.11, 0.92 ± 0.12, 0.92 ± 0.15, 1.01 ± 0.21, 1.10 ± 0.12, 1.50 ± 0.22, and 1.70 ± 0.21; by definition, the corresponding value for the observations is exactly 1.

Despite some large differences in specific cases, there is a general consistency between the values of s_U and the other coupling coefficients. For example, ordering the models by increasing value of s_U (as in Table 3) or by increasing value of the mean ratio of model-to-observed coupling coefficients produces the same result. From the ratios in Table 2, estimates of the four coupling coefficients, s_U, s_{Cu}, s_{str}, and s_{Cstr}, in the WRF_GBM experiment were all within 2%–8% of the corresponding QuikSCAT estimates; for the two divergence metrics s_{Du} and s_{Dstr}, however, WRF_GBM overestimated the QuikSCAT values by 23% and 26%, respectively. The WRF_MYJ simulation consistently underestimated the coupling coefficients by 6%–29%, while WRF_UW and WRF_MYNN2 both overestimated the QuikSCAT coupling coefficients by 27%–86% and 34%–97%, respectively. The COAMPS coupling coefficients were relatively larger for wind and divergence than for stress and curl.

Based on our primary metric s_U, the WRF_GBM experiment produced the wind field response to SST that is most consistent with the QuikSCAT observations of SST influence on the surface wind field, followed by COAMPS_ipbl = 2. One might say COAMPS_ipbl = 2 performed best based on the mean ratio of simulated to observed coupling coefficients, but its mean ratio results from compensating overestimates and underestimates of individual coefficient ratios. The six individual coupling coefficient ratios for COAMPS_ipbl = 2 had a standard deviation 1.75 times larger than the standard deviation for WRF_GBM.

c. *Boundary layer structure*

1) WIND AND THERMAL PROFILES

In addition to examining the response of the surface wind to SST, we analyzed the vertical structure of the model atmospheric boundary layer in the simulations. Profiles of average wind speed for all of the simulations over the nested domain (Fig. 9a) differ by a maximum of 1.1 m s^{-1} near the sea surface, and about 1.0–1.4 m s^{-1} at 150–1500 m. Average profiles of potential temperature (Fig. 9b) differ by up to 1.3 K near the sea surface, by somewhat more than 2.0 K at an elevation around 600 m, and by less than 1.0 K at elevations of 1500 m and higher.

TABLE 3. Summary of the coupling coefficients computed for different wind variables (see section 2e): s_U is for ENS wind–SST perturbations ($m\,s^{-1}\,°C^{-1}$); s_{Cu} is for ENS wind curl (relative vorticity)–crosswind SST gradient ($m\,s^{-1}\,°C^{-1}$); s_{Du} is for ENS wind divergence–downwind SST gradient ($m\,s^{-1}\,°C^{-1}$); s_{str} is for wind stress–SST perturbations ($N\,m^{-2}\,°C^{-1}$); s_{Cstr} is for wind stress curl–crosswind SST perturbations ($\times 100\,N\,m^{-2}\,°C^{-1}$); and s_{Dstr} is for wind stress divergence–downwind SST perturbations ($\times 100\,N\,m^{-2}\,°C^{-1}$). Ratios in data columns 7–12 are between the given coupling coefficient and its corresponding estimate from QuikSCAT (QuikSCAT + NOAA OI SST). Highlighted in boldface font are the row with QuikSCAT coupling coefficients and the column with the wind speed coupling coefficient s_U that is used in this study as the primary metric for assessment of air–sea coupling. Rows are ordered according to the magnitude of s_U for each model simulation.

Database	s_U	s_{Cu}	s_{Du}	s_{str}	s_{Cstr}	s_{Dstr}	$\frac{s_U}{s_{U\_QS}}$	$\frac{s_{Cu}}{s_{Cu\_QS}}$	$\frac{s_{Du}}{s_{Du\_QS}}$	$\frac{s_{str}}{s_{str\_QS}}$	$\frac{s_{Cstr}}{s_{Cstr\_QS}}$	$\frac{s_{Dstr}}{s_{Dstr\_QS}}$
WRF_MYJ	**0.31**	0.28	0.57	0.017	1.56	2.82	0.75	0.73	0.94	0.79	0.71	0.93
WRF_MYJ_SFCLAY	**0.34**	0.30	0.61	0.019	1.79	3.10	0.82	0.77	1.02	0.87	0.81	1.02
WRF_YSU	**0.35**	0.29	0.61	0.021	1.87	3.19	0.85	0.75	1.02	0.98	0.85	1.05
COAMPS_ipbl = 1	**0.36**	0.40	0.68	0.016	1.83	2.78	0.85	1.05	1.13	0.73	0.83	0.91
COAMPS_ipbl = 2	**0.38**	0.42	0.82	0.017	1.84	3.19	0.91	1.10	1.36	0.79	0.84	1.05
WRF_GBM	**0.40**	0.38	0.74	0.024	2.35	3.82	0.96	0.98	1.23	1.08	1.07	1.26
QuikSCAT v4	**0.42**	**0.39**	**0.60**	**0.022**	**2.20**	**3.04**	**1.00**	**1.00**	**1.00**	**1.00**	**1.00**	**1.00**
WRF_UW	**0.53**	0.53	1.03	0.033	3.54	5.66	1.27	1.38	1.70	1.49	1.61	1.86
WRF_MYNN2	**0.56**	0.66	1.05	0.035	3.97	6.00	1.34	1.70	1.75	1.61	1.80	1.97

The models differ significantly in their simulation of near-surface wind shear and stability (Figs. 9a,b), both of which affect the vertical transfer of momentum in the boundary layer. The WRF_UW experiment yields the most stable (nearly linear) potential temperature profile, and the strongest wind shear near the sea surface below 400 m. Vertical profiles of the wind speed coupling coefficients (Fig. 9c), estimated in a simplified manner using Eq. (7), indicate a dipole structure in which the sensitivity of wind speed to SST is highest near the sea surface ($0.19–0.44\,m\,s^{-1}\,°C^{-1}$), decreases rapidly with increasing height and crosses zero near 150–300 m for most models, and has a weak negative coupling near 300 m. There is virtually no sensitivity of the wind speed to SST above 600–800 m for any of the models. These profiles are consistent with SST-induced vertical transfer of momentum between the middle of the PBL and the sea surface. Coupling coefficients for potential temperature sensitivity to SST (Fig. 9d) show a significantly different picture in which high surface values ($0.38–0.50\,K\,°C^{-1}$) in all of the experiments decrease gradually and monotonically, but not approaching zero until 1000–1400 m.

Composite profiles of the wind response to SST for different SST perturbation ranges (Fig. 10) show stronger positive wind perturbations over warmer areas, and stronger negative wind perturbations (weakest winds) over colder patches. Consistent with the coupling-coefficient profiles (Fig. 9c), these wind perturbations are generally restricted to the lowest few hundred meters. Above 150–400 m, the models predict stronger winds in the most stable conditions over the coldest SST patches (<−1.5°C), but not over the intermediate range of moderately stable conditions over cooler SST perturbations (−1.5° ≤ SST′ ≤ −0.5°C). There is less agreement between the models on weakening of winds in the middle and upper part of the boundary layer in the most unstable conditions over the warmest SST perturbations (>1.5°C). All simulations show an asymmetrical response between the warm and cold patches, indicating an asymmetric response of turbulent mixing to modified sea–air stability. This results because the mixing coefficient K_M depends on the nonlinear stability function S_M [Eq.(1)] in the Mellor–Yamada-type schemes, and depends nonlinearly on stability through the Richardson number in the nonlocal-K schemes.

The modeled weakening of near-surface winds over cold water is expected if increased static stability permits an increasingly strong sheared layer in the lowest 400 m, depleted of momentum at the surface (Samelson et al. 2006). Some models have an excess of momentum above the stable layer due to the anomalous reduction of drag, analogous to the mechanism that produces nocturnal low-level jets (Small et al. 2008; Vihma et al. 1998).

2) VERTICAL TURBULENT DIFFUSION

To test the assumption that the differences between the coupling coefficients obtained from the models using different boundary layer schemes would be reflected in differences in the vertical mixing of momentum, we examined profiles of the eddy viscosity K_M from each of the model simulations. Spatial-mean profiles of time-mean K_M (Fig. 11, left panel) show elevated maxima at 350–500 m, varying from about 45 to $80\,m^2\,s^{-1}$, with one exception; the vertical structure of K_M is notably different for WRF_UW, with much higher values than the other seven models throughout the boundary layer above 400 m and a maximum of almost $140\,m^2\,s^{-1}$ at an

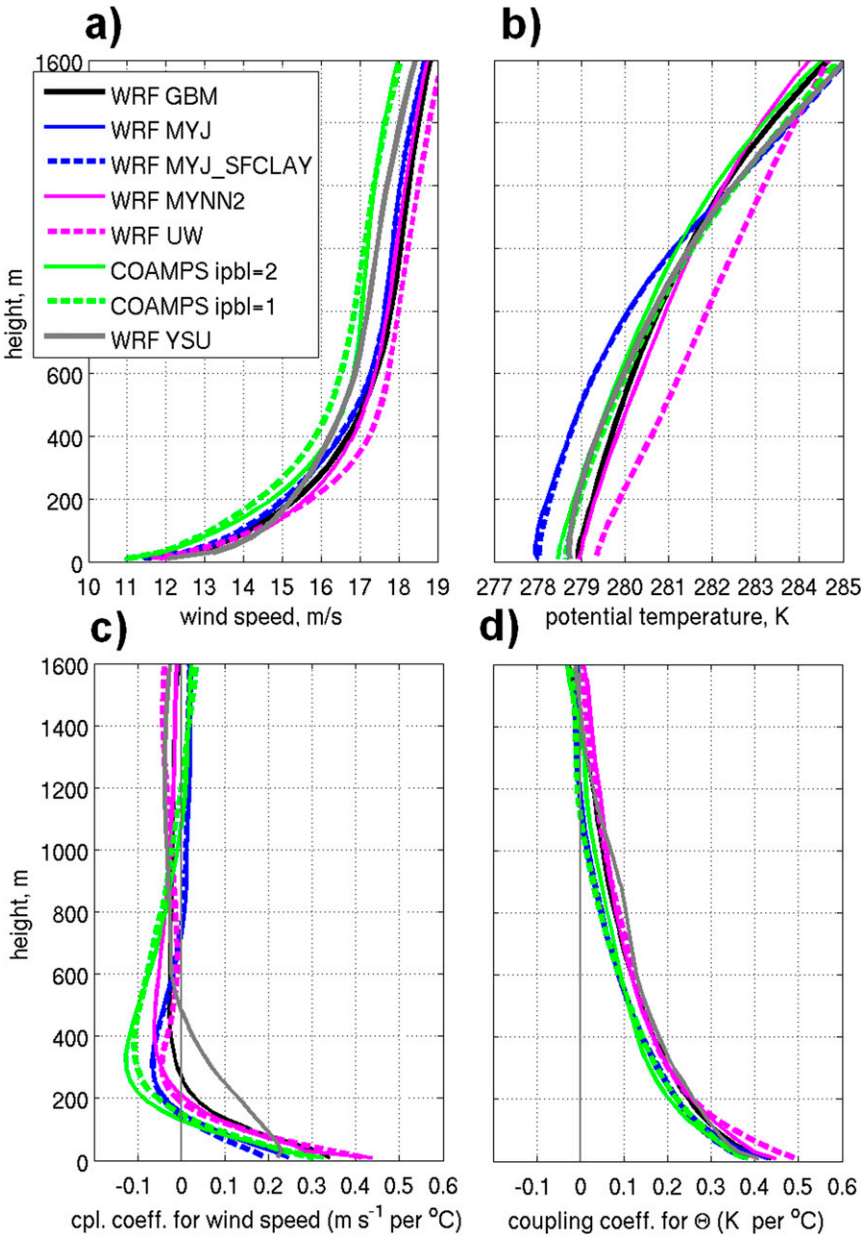

FIG. 9. Vertical profiles averaged over the nested domain for (a) average wind speed, (b) potential temperature, (c) coupling coefficients for the SST dependence of spatially high-pass-filtered wind speed at each level, and (d) coupling coefficients for the SST dependence of spatially high-pass-filtered potential temperature at each level.

elevation around 1500 m. Profiles of the spatial standard deviations of the time-averaged K_M perturbations (defined to be the K_M at each level after spatially high-pass filtering in the same manner as the filtering of the winds) are similar to the mean K_M profiles (Figs. 11a,b), with magnitudes that scale roughly with the mean K_M. The relative amplitudes of the mean and standard deviation K_M profiles (Figs. 11a,b) are generally consistent with the relative values of the coupling coefficients (Table 3), with the models that produce larger coupling coefficients tending also to have larger mean and perturbation K_M. This relation can be illustrated and quantified by computing the correlation ρ between and s_U and a height-averaged eddy viscosity K_M for the eight experiments in Table 1. For an average over 0–600 m, this yields ρ = 0.83 (Fig. 11c).

We carried out an additional experiment based on the WRF_GBM simulation in which the turbulent eddy

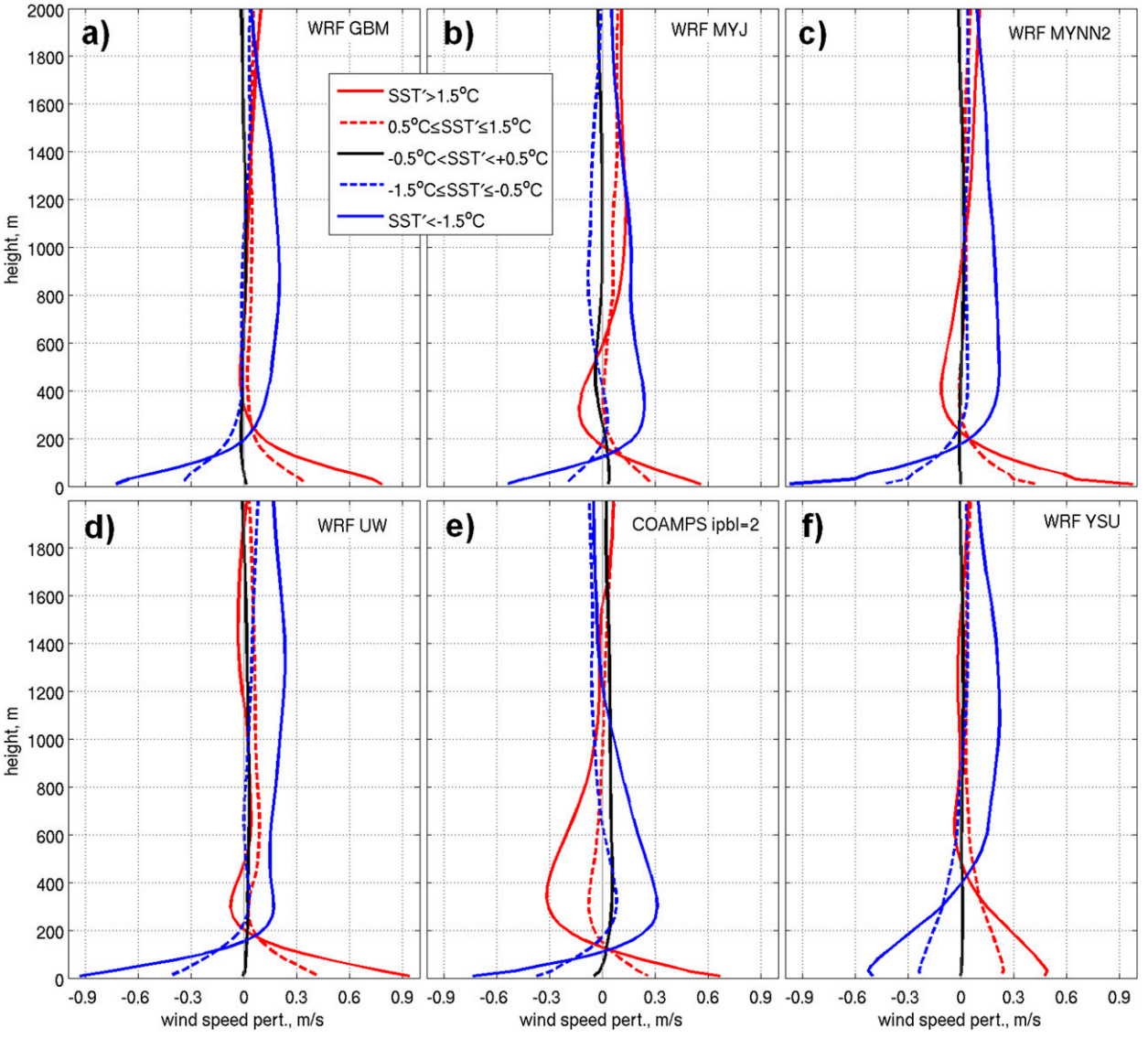

FIG. 10. Average profiles of spatially high-pass-filtered wind speed for ranges of SST perturbations, as indicated on the legend, for the following six simulations: (a) WRF GBM, (b) WRF MYJ, (c) WRF MYNN2, (d) WRF UW, (e) COAMPS ipbl = 2, and (f) WRF YSU.

transfer coefficients (K_M and K_H) were set constant in time and location, and identical to the average profile from WRF_GBM in Fig. 11a. The turbulent mixing in this simulation was therefore invariant to the actual atmospheric stability. The resulting coupling coefficient was only 0.15 m s^{-1} °C^{-1} (the point labeled "K_m, K_h fixed" in Fig. 11c). This experiment indicates that representation of the stability dependence of parameterized eddy transfer is essential in order to produce an accurate model estimate of air–sea coupling.

Song et al. (2009) previously reported a strong relation between s_U and the stability dependence of vertical diffusion in WRF simulations that compared the GB01 PBL scheme (an earlier version of the GBM PBL scheme, as discussed in the introduction) and the WRF_MYJ PBL scheme. Song et al. (2009) introduced a "stability factor" R_s to investigate the effects of the stability functions S_M, S_H on the turbulent eddy mixing coefficients $K_{M,H} = lqS_{M,H}$ [Eq. (1)]. The stability functions S_M, S_H were scaled with this stability factor R_s as follows:

$$\tilde{S} = S^N + R_s(S - S^N), \tag{8}$$

where S is the stability function for momentum (S_M) or heat (S_H) evaluated by the model scheme for the prevailing conditions, and S^N is the same model stability function evaluated for neutrally stable conditions. A

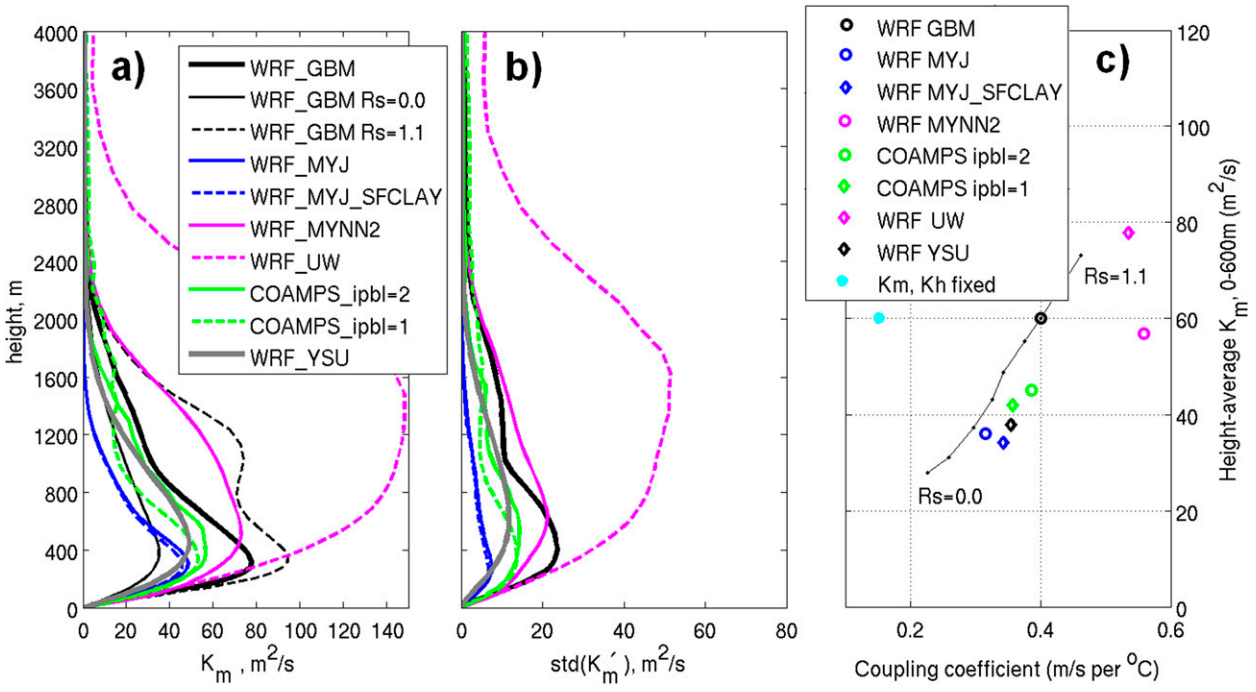

FIG. 11. (a) Vertical profiles of monthly average eddy viscosity coefficients K_M for the nested domain and (b) vertical profiles of the standard deviations of monthly average perturbation of K_M for eight model simulations. (c) The 0–600-m vertically averaged K_M vs the coupling coefficient. The black line in (c) corresponds to WRF_GBM simulations with modified stability response factors of $R_s = 0.0, 0.1, 0.3, 0.5, 0.7, 0.9, 1.0$, and 1.1 (only the first and last numbers are labeled). The cyan point with very small coupling coefficient corresponds to the simulation using WRF_GBM, but with the turbulent eddy viscosity and diffusivity profiles invariant and fixed to the domain average of the K_M profile for WRF_GBM shown in (a).

value of $R_s = 0$ thus effectively removes the stability dependence, while $R_s = 1$ is equivalent to the original GB01 scheme. The modified stability functions $\tilde{S}_M$ and $\tilde{S}_H$ were then used in the equations for the turbulent eddy coefficient for momentum and heat. In the case of Song et al. (2009), $R_s = 1$ gave the GB01 scheme estimated by Eqs. (24) and (25) from Galperin et al. (1988). Song et al. (2009) found that reducing the stability parameter R_s below 1 consistently lowered the coupling coefficient; attempts to increase the R_s, however, rapidly led to mixing that was too strong, resulting in unstable model behavior.

We conducted additional experiments following this modified stability-parameter approach for the WRF_GBM scheme. The profiles of K_M shown in Fig. 11a for values of $R_s = 0$ and $R_s = 1$ (equivalent to WRF_MYJ and WRF_GBM, respectively) and $R_s = 1.1$ show a systematic increase of K_M with increasing R_s. Profiles of K_M for $R_s = 0.1, 0.3, 0.5, 0.7$, and 0.9 (not shown here) vary gradually between those with $R_s = 0$ and $R_s = 1$, and all showed a single elevated maximum. Increasing the stability with $R_s = 1.1$ produced excessive mixing in the boundary layer (though not nearly as strong as WRF_UW), with a secondary maximum at an elevation of about 1200 m. Examination of the individual K_M profiles for the different values of R_s suggests that the simulations that have a stronger maximum of K_M also have a higher wind speed coupling coefficient. The sensitivity experiments resulted in consistently higher coupling coefficients s_U with increasing R_s and the static stability had more influence on the vertical mixing. The simulation with $R_s = 1$ resulted in a coupling coefficient for 10-m ENS winds that was the closest to the QuikSCAT estimate. For $R_s = 0.0$, the coupling coefficient was too small by almost 60%. These results are consistent with those obtained by Song et al. (2009) with the GB01 PBL scheme.

The sensitivity of the K_M profiles to SST in the standard WRF_GBM experiment with $R_s = 1$ was studied in two different ways (Fig. 12). We calculated vertical profiles of K_m anomalies, defined as deviations of the modeled values from their temporal and spatial average at each vertical level. In the first method, the monthly average vertical profiles of K_M perturbations were grouped by the local SST perturbations (Fig. 12, left panel). In the second method, instantaneous profiles of K_M anomalies at each time step of the simulation were grouped according to the orientation of the surface wind vector relative to the SST gradient (Fig. 12, right panel). The calculations were done for every individual time step because the wind direction changed over the 30-day simulation. The grouped instantaneous profiles in the

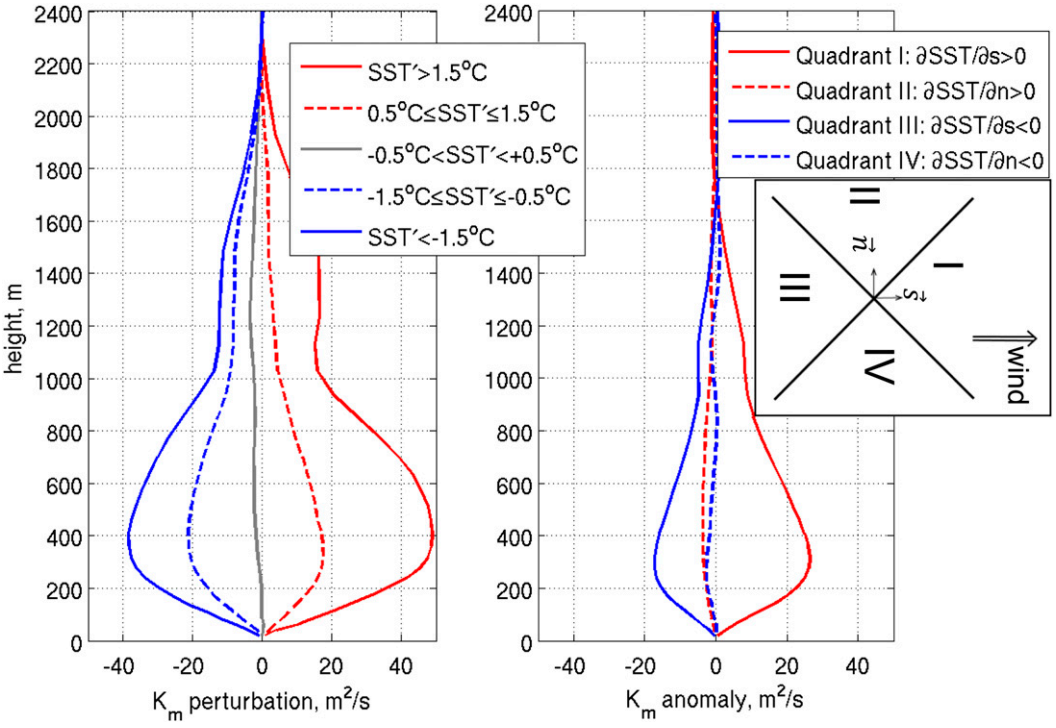

FIG. 12. (left) Average profiles of eddy viscosity anomalies K'_M from the WRF_GBM simulation for different SST perturbation ranges, where the anomaly of K_M was determined at each level as the departure from the average at that level. (right) Monthly mean K_M anomaly for different orientations of the surface wind vector relative to the SST gradient, where the anomaly at each level was determined as the departure from the time- and domain-averaged K_M at that level for each time step of the model simulations, after which the monthly average was computed. The vectors **s** and **n** are unit vectors in the downwind and crosswind directions, respectively (see the insert for details). Quadrants I, II, III, and IV are determined from downwind $\partial\text{SST}/\partial s$ and crosswind $\partial\text{SST}/\partial n$ components, as follows. Quadrant I: $\partial\text{SST}/\partial s > 0$ and $|\partial\text{SST}/\partial s| > |\partial\text{SST}/\partial n|$ (wind blows predominantly along the SST gradient, from cold to warm water); Quadrant II: $\partial\text{SST}/\partial n > 0$ and $|\partial\text{SST}/\partial n| > |\partial\text{SST}/\partial s|$ (wind blows across the SST gradient, with warmer water to the left of the wind direction); Quadrant III: $\partial\text{SST}/\partial s < 0$ and $|\partial\text{SST}/\partial s| > |\partial\text{SST}/\partial n|$ (wind blows in the direction opposite the SST gradient, from warm to cold water); and Quadrant IV: $\partial\text{SST}/\partial n < 0$ and $|\partial\text{SST}/\partial n| > |\partial\text{SST}/\partial s|$ (wind blows across the SST gradient, with warmer water to the right of the wind direction).

second method were then averaged to obtain the profiles in the right panel of Fig. 12.

In the first method, the warmest patches (>1.5°C) resulted in more than a 55% increase in peak values at about 350–400 m compared with the average profile in Fig. 11a. The coldest SST patches (<−1.5°C) yielded a reduction of 50% from the peak average values. A consistent increase in vertical mixing over the warmest patches occurred over the upper portion of the boundary layer as well, between elevations of 1000–2000 m, where reduction of mixing is less for the cold patches. This could be due to deepening of the boundary layer over the warmest SST perturbations.

The analysis using the second method indicates a clear tendency of increased vertical mixing and higher K_M by about 30% at ~300 m when surface winds blow predominantly along the SST gradient toward warmer SST, and a decrease of about 20% when winds blow in the opposite direction (i.e., toward colder SST). No significant changes in eddy viscosity profiles were found for the cases of winds blowing perpendicular to SST gradients (i.e., parallel to isotherms). The effect of relative direction on the profiles of K_M decreases with increasing elevation above 300 m and becomes negligible above 1600 m.

Because of the strong effect of local SST changes on vertical mixing (Fig. 12, left), we further quantified the sensitivity of turbulent eddy viscosity K_M to SST perturbations for the various models by bin averaging the 0–600-m height-averaged K_M perturbations as a function of SST perturbation (Fig. 13). Height-average K_M perturbations were most sensitive in the WRF_GBM, WRF_MYNN2, and WRF_UW simulations, with WRF_UW having the most extreme sensitivity. The

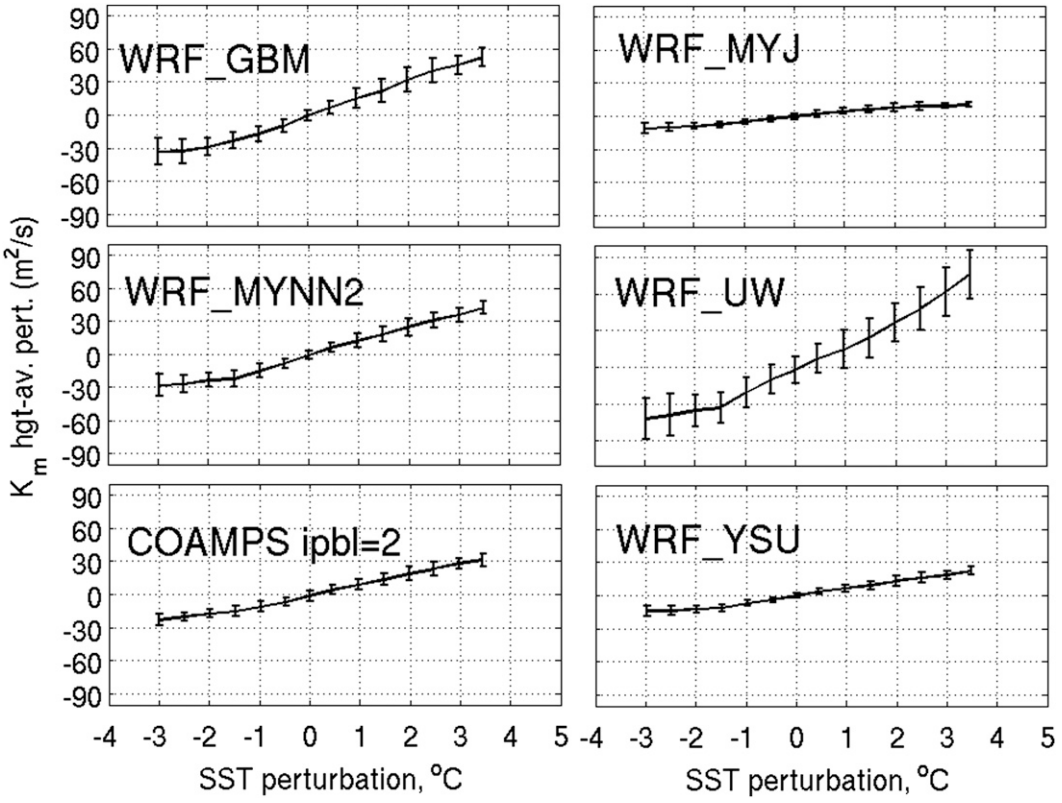

FIG. 13. Sensitivity of 0–600-m height-averaged eddy viscosity perturbations K'_M to binned SST perturbations, for the six models labeled in each panel, computed using a method similar to the wind speed coupling coefficients. The error bars indicate ±1 standard deviation from the mean value for each bin.

COAMPS_ipbl = 2 and WRF_YSU simulations had much weaker sensitivity, and WRF_MYJ had the weakest sensitivity. The variability between the models is substantial not only in the rate of K_M increase per temperature perturbation (°C), but also in the standard deviations of the K_M perturbations within each binned value of SST. For all of the experiments except WRF_MYJ, the rate of increase is slightly lower for negative SST perturbations, and higher for positive SST perturbations. This is in agreement with Fig. 12 (left), in which warmer SST patches produced eddy viscosity gain not only in the lower levels where the K_M is largest, but in the upper portion of the boundary layer (between 1000 and 2000 m) as well.

4. Summary and discussion

Our numerical modeling study explores the sensitivity to the choice of vertical mixing parameterization of the SST influence on the atmospheric boundary layer in the region of Agulhas Return Current (ARC). Month-long simulations were conducted for July 2002 using eight different combinations of state-of-the-art boundary layer mixing schemes and mesoscale atmospheric models (WRF and COAMPS). The performance of each simulation was assessed by how closely it reproduced the response of the surface wind fields to SST deduced from satellite data.

The primary metric for model performance in our study is the coupling coefficient between equivalent neutral stability (ENS) wind speed and SST. We advocate this metric for comparing atmospheric and coupled ocean–atmosphere models to satellite observations because it is less sensitive than the coupling coefficient for wind stress to seasonal and large-scale changes in the background mean winds (O'Neill et al. 2012). The coupling coefficient computed for QuikSCAT measurements of ENS wind speed is $0.42\,\mathrm{m\,s^{-1}\,°C^{-1}}$. The ENS winds from the eight model simulations resulted in coupling coefficients ranging from 0.31 to $0.56\,\mathrm{m\,s^{-1}\,°C^{-1}}$.

We also investigated the vertical structures of mesoscale wind and potential temperature response to SST from the simulations. The sensitivity of potential temperature perturbations to SST perturbations was strong near the sea surface (0.38–$0.50\,\mathrm{K\,°C^{-1}}$) and decreased rapidly with elevation in the lower 200 m, and then more

gradually up to about 1400 m. Wind speed sensitivity to SST near the surface (0.19–0.44 m s^{-1} °C^{-1}) decreased rapidly to near zero at 150–300 m, and then became weakly negative at about 150–500 m for the experiments with Mellor–Yamada-type PBL schemes. ["Mellor–Yamada type" refers to the family of schemes that parameterize eddy diffusivities as a function of TKE of the form of Eq. (1).] The change in sign of the coupling between the surface and the middle of the boundary layer is consistent with the vertical exchange of momentum expected from SST influence on vertical mixing.

Among the eight mixing parameterizations considered, the newly implemented Grenier–Bretherton–McCaa (GBM) boundary layer mixing scheme in the WRF Model produced a wind speed coupling coefficient of 0.40 m s^{-1} °C^{-1} that is the closest to the estimate from QuikSCAT observations. Additionally, the WRF_GBM simulations showed the best consistency with QuikSCAT for three of the other five coupling metrics considered in our analysis. Namely, the estimates from the WRF_GBM simulation were within 2%–8% of their corresponding QuikSCAT estimates for the wind stress magnitude, wind vorticity, and wind stress curl responses to the underlying SST field. Although it overestimated the wind and wind stress divergence responses, the GBM PBL scheme compared the best overall with the QuikSCAT observations. The computer code for our implementation of GBM mixing is now distributed with WRF versions subsequent to version 3.5.

The COAMPS experiment with the ipbl = 2 Mellor–Yamada-type boundary layer scheme produced a slightly lower value of the wind speed coupling coefficient, 0.38 m s^{-1} °C^{-1}, only slightly smaller than the WRF_GBM coupling coefficient. Based on the mean modeled-to-observed ratios of all six coupling coefficients, the COAMPS_ipbl = 2 simulation performed better than any other simulation, including WRF_GBM. However, with the exception of wind stress divergence, the departures from the QuikSCAT values of the individual coupling coefficients were all larger in magnitude for COAMPS_ipbl = 2 than for WRF_GBM. Also, COAMPS_ipbl = 2 (as well as COAMPS_ipbl = 1) underestimated the large-scale ENS winds compared with the QuikSCAT observations and with all of the WRF experiments. This could be due to the use of the global NCEP FNL reanalysis model for initial and boundary conditions in all of our model experiments. Use of initial and boundary conditions from the U.S. Navy's Operational Global Atmospheric Prediction System (NOGAPS) model, the standard source for developmental and operational implementations of COAMPS, might have produced different results.

A perhaps surprising result of this study is that the seven simulations with Mellor–Yamada-type vertical mixing schemes of the form in Eq. (1) yield widely varying coupling coefficients, with extreme values of s_U differing by nearly a factor of 2 (Table 3). In an effort to understand this, we looked in detail at the various implementations of the equation for K_M [Eq. (1)] and the resulting model values for the eddy viscosity K_M in the lower atmosphere. Vertical profiles of K_M were found to depend strongly on the underlying mesoscale SST variability: the coldest patches with SST perturbations <-1.5°C resulted in a decrease of K_M by up to 50%, implying decreased mixing in the presence of shear below 350–400 m. The warmest SST patches (>1.5°C SST perturbations) resulted in an increase of K_M by as much as 55%, as well as additional increase in the mixing between 1000 and 1200 m. The latter result is consistent with deepening of the boundary layer over the warmer areas.

The relative orientation of the surface wind vector and the underlying SST the gradient affected vertical mixing profiles as well; higher values of K_M by up to 30% of the mean were found within the boundary layer for flow from cold to warm water (i.e., in the direction of the SST gradient), and lower values of up to 20% were found for flow from warm to cold water (counter to the SST gradient). Overall, the diagnosed 0–600-m height-averaged turbulent eddy viscosity K_M was found to be well correlated ($\rho = 0.83$) with the coupling coefficients for the eight model experiments in Table 3. This further implicates the importance of vertical mixing in the lower part of the boundary layer to this air–sea interaction process.

With the importance of variations in K_M established, we attempted to identify the key parameters in the different formulations and implementations of Eq. (1) that affected the atmospheric response to the SST variability. Static stability, wind shear parameters (used in calculations of stability functions S_M and S_H), turbulent kinetic energy (TKE), turbulent master length scale l, and eddy transfer coefficient K_q for TKE in Mellor–Yamada schemes, all showed notable variations between the model simulations. For example, the WRF and COAMPS schemes use different estimates for the turbulent mixing master length l and different forms for the stability functions $S_{M,H}$. Furthermore, the two formulations use different numerical techniques for computing vertical gradients, which in turn affects the estimate of the stability parameters $S_{M,H}$. Since vertical gradients are strong near the sea surface, small details in the numerical techniques can have large effects on the resulting estimates of $S_{M,H}$. The different values of l and $S_{M,H}$ in the various models with Mellor–Yamada-type mixing apparently account for the wide range of coupling

coefficients. However, these differences themselves can have different effects on K_M, depending on the implementation of the TKE equation [Eq. (2)]. Ultimately, no single parameter was clearly identifiable as a performance metric or dominant control for the SST response.

Surprisingly, the results of WRF_UW simulation were very different from the GBM simulation. The UW PBL scheme is an implementation of the GB01 boundary layer mixing scheme, simplified and adapted for use in climate models with longer time steps. The GBM PBL scheme evolved from the GB01 boundary layer mixing scheme. Despite their shared heritage, the WRF_UW simulation produced a wind speed coupling coefficient of $0.53\,\mathrm{m\,s^{-1}\,°C^{-1}}$ that is much higher than the value of $0.40\,\mathrm{m\,s^{-1}\,°C^{-1}}$ obtained from the WRF_GBM simulation. All of the other coupling coefficients from the WRF_UW experiment were similarly larger in comparison with those from the WRF_GBM experiment. It worth mentioning, however, that the UW PBL scheme in the CAM5 global model has been found to produce a wind speed coupling coefficient for the same geographical region (the ARC) that is quite close to the observed value obtained from QuikSCAT (R. J. Small 2013, personal communication). There is no clear explanation yet on why the UW PBL scheme appears to perform so differently in WRF and CAM5.

Perhaps the most important conclusion of this study is that the choice of PBL mixing parameterization for a given atmospheric model (or coupled-model component) must be given careful consideration, because the coupling coefficients depends strongly on that choice, as illustrated by their differences for the various characterizations of the surface wind field and the eight different PBL schemes considered in this study (Table 3). Since the horizontal grid spacing in the mesoscale model simulations carried out for this study is comparable to the grid spacing in operational global forecast models, the results presented here are relevant to the global models, which are known to underestimate surface wind response to SST (Chelton and Wentz 2005; Song et al. 2009; Chelton and Xie 2010). It is important that this air–sea interaction be accurately represented in models, since the wind response to mesoscale SST is coupled to other changes in the boundary layer (e.g., clouds that can arise from surface wind convergence) (Minobe et al. 2008; Young and Sikora 2003). It is especially important that the surface wind response to SST be accurately represented in coupled models in order to reproduce accurately the SST-induced wind stress curl perturbations that feedback on the ocean circulation, which in turn alters the SST that then perturbs the surface wind field. This two-way coupling cannot be accurately represented if the surface wind response to SST is under- or overestimated by the atmospheric component of the coupled model.

Acknowledgments. This research has been supported by the NASA Grants NNX10AE91G and NNX10A098G. We thank Qingtao Song for providing the codes from his 2009 modeling study that we adapted for the WRF simulation in the present study. We are also grateful to Justin Small (NCAR) for methodical discussions about the coupling coefficients and for sharing the findings of his group.

REFERENCES

Beljaars, A. C. M., 1995: The parameterization of surface fluxes in large-scale models under free convection. *Quart. J. Roy. Meteor. Soc.,* **121,** 255–270, doi:10.1002/qj.49712152203.

Bretherton, C. S., and S. Park, 2009: A new moist turbulence parameterization in the Community Atmosphere Model. *J. Climate,* **22,** 3422–3448, doi:10.1175/2008JCLI2556.1.

——, J. R. McCaa, and H. Grenier, 2004: A new parameterization for shallow cumulus convection and its application to marine subtropical cloud-topped boundary layers. Part I: Description and 1D results. *Mon. Wea. Rev.,* **132,** 864–882, doi:10.1175/1520-0493(2004)132<0864:ANPFSC>2.0.CO;2.

Cayan, D. R., 1992: Latent and sensible heat flux anomalies over the northern oceans: Driving the sea surface temperature. *J. Phys. Oceanogr.,* **22,** 859–881, doi:10.1175/1520-0485(1992)022<0859:LASHFA>2.0.CO;2.

Charnock, H., 1955: Wind stress on a water surface. *Quart. J. Roy. Meteor. Soc.,* **81,** 639–640, doi:10.1002/qj.49708135027.

Chelton, D. B., and M. G. Schlax, 2003: The accuracies of smoothed sea surface height fields constructed from tandem altimeter datasets. *J. Atmos. Oceanic Technol.,* **20,** 1276–1302, doi:10.1175/1520-0426(2003)020<1276:TAOSSS>2.0.CO;2.

——, and F. J. Wentz, 2005: Global high-resolution satellite observations of sea-surface temperature for numerical weather prediction and climate research. *Bull. Amer. Meteor. Soc.,* **86,** 1097–1115, doi:10.1175/BAMS-86-8-1097.

——, and S.-P. Xie, 2010: Coupled ocean-atmosphere interaction at oceanic mesoscales. *Oceanography,* **23,** 52–69, doi:10.5670/oceanog.2010.05.

——, and Coauthors, 2001: Observations of coupling between surface wind stress and sea surface temperature in the eastern tropical Pacific. *J. Climate,* **14,** 1479–1498, doi:10.1175/1520-0442(2001)014<1479:OOCBSW>2.0.CO;2.

——, M. Schlax, M. Freilich, and R. Milliff, 2004: Satellite measurements reveal persistent small-scale features in ocean winds. *Science,* **303,** 978–983, doi:10.1126/science.1091901.

——, M. G. Schlax, and R. M. Samelson, 2007: Summertime coupling between sea surface temperature and wind stress in the California Current System. *J. Phys. Oceanogr.,* **37,** 495–517, doi:10.1175/JPO3025.1.

Cleveland, W. S., and S. J. Devlin, 1988: Locally-weighted regression: An approach to regression analysis by local fitting. *J. Amer. Stat. Assoc.,* **83,** 596–610, doi:10.1080/01621459.1988.10478639.

Ducet, N., P.-Y. Le Traon, and G. Reverdin, 2000: Global high resolution mapping of ocean circulation from TOPEX/

POSEIDON and ERS-1/2. *J. Geophys. Res.,* **105,** 19 477–19 498, doi:10.1029/2000JC900063.

Dyer, A. J., and B. B. Hicks, 1970: Flux-gradient relationships in the constant flux layer. *Quart. J. Roy. Meteor. Soc.,* **96,** 715–721, doi:10.1002/qj.49709641012.

Fairall, C. W., E. F. Bradley, D. P. Rogers, J. B. Edson, and G. S. Young, 1996: Bulk parameterization of air-sea fluxes for TOGA COARE. *J. Geophys. Res.,* **101,** 3747–3764, doi:10.1029/95JC03205.

Frankignoul, C., 1985: Sea surface temperature anomalies, planetary waves, and air-sea feedback in the middle latitudes. *Rev. Geophys.,* **23,** 357–390, doi:10.1029/RG023i004p00357.

Galperin, B., L. H. Kantha, S. Hassid, and A. Rosati, 1988: A quasi-equilibrium turbulent energy model for geophysical flows. *J. Atmos. Sci.,* **45,** 55–62, doi:10.1175/1520-0469(1988)045<0055:AQETEM>2.0.CO;2.

Grenier, H., and C. S. Bretherton, 2001: A moist PBL parameterization for large-scale models and its application to subtropical cloud-topped marine boundary layers. *Mon. Wea. Rev.,* **129,** 357–377, doi:10.1175/1520-0493(2001)129<0357:AMPPFL>2.0.CO;2.

Haack, T., D. Chelton, J. Pullen, J. D. Doyle, and M. Schlax, 2008: Summertime influence of SST on surface wind stress off the U.S. West Coast from the U.S. Navy COAMPS model. *J. Phys. Oceanogr.,* **38,** 2414–2437, doi:10.1175/2008JPO3870.1.

Hodur, R. M., 1997: The Naval Research Laboratory's Coupled Ocean/Atmosphere Mesoscale Prediction System (COAMPS). *Mon. Wea. Rev.,* **125,** 1414–1430, doi:10.1175/1520-0493(1997)125<1414:TNRLSC>2.0.CO;2.

Hong, S.-Y., and H.-L. Pan, 1996: Nonlocal boundary layer vertical diffusion in a medium-range forecast model. *Mon. Wea. Rev.,* **124,** 2322–2339, doi:10.1175/1520-0493(1996)124<2322:NBLVDI>2.0.CO;2.

——, Y. Noh, and J. Dudhia, 2006: A new vertical diffusion package with an explicit treatment of entrainment processes. *Mon. Wea. Rev.,* **134,** 2318–2341, doi:10.1175/MWR3199.1.

Janjić, Z. I., 1994: The step-mountain Eta coordinate model: Further developments of the convection, viscous sublayer, and turbulence closure schemes. *Mon. Wea. Rev.,* **122,** 927–945, doi:10.1175/1520-0493(1994)122<0927:TSMECM>2.0.CO;2.

——, 1996: The surface layer in the NCEP Eta Model. Preprints, *11th Conf. on Numerical Weather Prediction,* Norfolk, VA, Amer. Meteor. Soc., 354–355.

——, 2002: Nonsingular implementation of the Mellor-Yamada level 2.5 scheme in the NCEP Meso Model. NCEP Office Note 437, 61 pp.

Liu, W. T., and W. Tang, 1996: Equivalent neutral wind. JPL Publ. 96-17, NASA Jet Propulsion Laboratory, 20 pp.

Louis, J., 1979: A parametric model of vertical eddy fluxes in the atmosphere. *Bound.-Layer Meteor.,* **17,** 187–202, doi:10.1007/BF00117978.

Maloney, E. D., and D. B. Chelton, 2006: An assessment of the sea surface temperature influence on surface wind stress in numerical weather prediction and climate models. *J. Climate,* **19,** 2743–2762, doi:10.1175/JCLI3728.1.

Mantua, N. J., S. R. Hare, Y. Zhang, J. M. Wallace, and R. C. Francis, 1997: A Pacific interdecadal climate oscillation with impacts on salmon production. *Bull. Amer. Meteor. Soc.,* **78,** 1069–1079, doi:10.1175/1520-0477(1997)078<1069:APICOW>2.0.CO;2.

Mellor, G., and T. Yamada, 1974: A hierarchy of turbulence closure models for planetary boundary layers. *J. Atmos. Sci.,* **31,** 1791–1806, doi:10.1175/1520-0469(1974)031<1791:AHOTCM>2.0.CO;2.

——, and ——, 1982: Development of a turbulence closure model for geophysical fluid problems. *Rev. Geophys.,* **20,** 851–875, doi:10.1029/RG020i004p00851.

Minobe, S., A. Kuwano-Yoshida, N. Komori, S.-P. Xie, and R. J. Small, 2008: Influence of the Gulf Stream on the troposphere. *Nature,* **452,** 206–210, doi:10.1038/nature06690.

Monin, A. S., and A. M. Obukhov, 1954: Basic laws of turbulent mixing in the surface layer of the atmosphere. *Tr. Akad. Nauk SSSR Geofiz. Inst.,* **24,** 163–187.

Nakanishi, M., and H. Niino, 2004: An improved Mellor–Yamada level-3 model with condensation physics: Its design and verification. *Bound.-Layer Meteor.,* **112,** 1–31, doi:10.1023/B:BOUN.0000020164.04146.98.

——, and ——, 2006: An improved Mellor–Yamada level-3 model: Its numerical stability and application to a regional prediction of advection fog. *Bound.-Layer Meteor.,* **119,** 397–407, doi:10.1007/s10546-005-9030-8.

O'Neill, L. W., 2012: Wind speed and stability effects on the coupling between surface wind stress and SST observed from buoys and satellite. *J. Climate,* **25,** 1544–1569, doi:10.1175/JCLI-D-11-00121.1.

——, D. B. Chelton, and S. K. Esbensen, 2003: Observations of SST-induced perturbations on the wind stress field over the Southern Ocean on seasonal time scales. *J. Climate,* **16,** 2340–2354, doi:10.1175/2780.1.

——, ——, ——, and F. J. Wentz, 2005: High-resolution satellite measurements of the atmospheric boundary layer response to SST variations along the Agulhas Return Current. *J. Climate,* **18,** 2706–2723, doi:10.1175/JCLI3415.1.

——, ——, and ——, 2010a: The effects of SST-induced surface wind speed and direction gradients on midlatitude surface vorticity and divergence. *J. Climate,* **23,** 255–281, doi:10.1175/2009JCLI2613.1.

——, S. K. Esbensen, N. Thum, R. M. Samelson, and D. B. Chelton, 2010b: Dynamical analysis of the boundary layer and surface wind responses to mesoscale SST perturbations. *J. Climate,* **23,** 559–581, doi:10.1175/2009JCLI2662.1.

——, D. B. Chelton, and S. K. Esbensen, 2012: Covariability of surface wind and stress responses to sea surface temperature fronts. *J. Climate,* **25,** 5916–5942, doi:10.1175/JCLI-D-11-00230.1.

Paulson, C. A., 1970: The mathematical representation of wind speed and temperature profiles in the unstable atmospheric surface layer. *J. Appl. Meteor.,* **9,** 857–861, doi:10.1175/1520-0450(1970)009<0857:TMROWS>2.0.CO;2.

Perlin, N., R. M. Samelson, and D. B. Chelton, 2004: Scatterometer and model wind and wind stress in the Oregon–California coastal zone. *Mon. Wea. Rev.,* **132,** 2110–2129, doi:10.1175/1520-0493(2004)132<2110:SAMWAW>2.0.CO;2.

Reynolds, R. W., T. M. Smith, C. Liu, D. B. Chelton, K. S. Casey, and M. G. Schlax, 2007: Daily high-resolution-blended analyses for sea surface temperature. *J. Climate,* **20,** 5473–5496, doi:10.1175/2007JCLI1824.1.

Ricciardulli, L., and F. J. Wentz, 2011: Reprocessed QuikSCAT (V04) wind vectors with Ku-2011 geophysical model function. Remote Sensing Systems Rep. 043011, Santa Rosa, CA, 8 pp.

Rio, M.-H., and F. Hernandez, 2004: A mean dynamic topography computed over the world ocean from altimetry, in situ measurements, and a geoid model. *J. Geophys. Res.,* **109,** C12032, doi:10.1029/2003JC002226.

——, P. Schaeffer, F. Hernandez, and J.-M. Lemoine, 2005: The estimation of the ocean Mean Dynamic Topography

through the combination of altimetric data, in-situ measurements and GRACE geoid: From global to regional studies. *Proc. GOCINA Int. Workshop,* Kirchberg, Luxembourg, European Space Agency.

Ross, D. B., V. J. Cardone, J. Overland, R. D. McPherson, W. J. Pierson Jr., and T. Yu, 1985: Oceanic surface winds. *Advances in Geophysics,* Vol. 27, Academic Press, 101–138.

Samelson, R. M., E. D. Skyllingstad, D. B. Chelton, S. K. Esbensen, L. W. O'Neill, and N. Thum, 2006: On the coupling of wind stress and sea surface temperature. *J. Climate,* **19,** 1557–1566, doi:10.1175/JCLI3682.1.

Schlax, M. G., and D. B. Chelton, 1992: Frequency domain diagnostics for linear smoothers. *J. Amer. Stat. Assoc.,* **87,** 1070–1081, doi:10.1080/01621459.1992.10476262.

Skamarock, W. C., J. B. Klemp, J. Dudhia, D. O. Gill, D. M. Barker, W. Wang, and J. G. Powers, 2005: A description of the advanced research WRF version 2. NCAR Tech. Note NCAR/TN-468+STR, 88 pp. [Available online at http://www.mmm.ucar.edu/wrf/users/docs/arw_v2.pdf.]

Small, R. J., and Coauthors, 2008: Air–sea interaction over ocean fronts and eddies. *Dyn. Atmos. Oceans,* **45,** 274–319, doi:10.1016/j.dynatmoce.2008.01.001.

Song, Q., D. B. Chelton, S. K. Esbensen, N. Thum, and L. W. O'Neill, 2009: Coupling between sea surface temperature and low-level winds in mesoscale numerical models. *J. Climate,* **22,** 146–164, doi:10.1175/2008JCLI2488.1.

Stull, R. B., 1988: *An Introduction to Boundary Layer Meteorology.* Kluwer Academic Publishers, xiii + 666 pp.

Troen, I., and L. Mahrt, 1986: A simple model of the atmospheric boundary layer: Sensitivity to surface evaporation. *Bound.-Layer Meteor.,* **37,** 129–148, doi:10.1007/BF00122760.

Uno, I., X.-M. Cai, D. G. Steyn, and S. Emori, 1995: A simple extension of the Louis method for rough surface layer modelling. *Bound.-Layer Meteor.,* **76,** 395–409, doi:10.1007/BF00709241.

Vihma, T., J. Uotila, and J. Launiainen, 1998: Air–sea interaction over a thermal marine front in the Denmark Strait. *J. Geophys. Res.,* **103,** 27 665–27 678, doi:10.1029/98JC02415.

Wang, S., Q. Wang, and J. D. Doyle, 2002: Some improvement to Louis surface flux parameterization. *15th Conf. on Boundary Layer and Turbulence,* Wageningen, Netherlands, Amer. Meteor. Soc., 13.3a. [Available online at https://ams.confex.com/ams/BLT/techprogram/paper_44519.htm.]

Webb, E. K., 1970: Profile relationships: The log-linear range, and extension to strong stability. *Quart. J. Roy. Meteor. Soc.,* **96,** 67–90, doi:10.1002/qj.49709640708.

Xie, S.-P., 2004: Satellite observations of cool ocean–atmosphere interaction. *Bull. Amer. Meteor. Soc.,* **85,** 195–208, doi:10.1175/BAMS-85-2-195.

Yamada, T., 1983: Simulations of nocturnal drainage flows by a q^2l turbulence closure model. *J. Atmos. Sci.,* **40,** 91–106, doi:10.1175/1520-0469(1983)040<0091:SONDFB>2.0.CO;2.

Young, G. S., and T. D. Sikora, 2003: Mesoscale stratocumulus bands caused by Gulf Stream meanders. *Mon. Wea. Rev.,* **131,** 2177–2191, doi:10.1175/1520-0493(2003)131<2177:MSBCBG>2.0.CO;2.

Zhang, D., and R. A. Anthes, 1982: A high-resolution model of the planetary boundary layer—Sensitivity tests and comparisons with SESAME-79 data. *J. Appl. Meteor.,* **21,** 1594–1609, doi:10.1175/1520-0450(1982)021<1594:AHRMOT>2.0.CO;2.

Zhang, G. J., and N. A. McFarlane, 1995: Sensitivity of climate simulations to the parameterization of cumulus convection in the Canadian Climate Centre general circulation model. *Atmos.–Ocean,* **33,** 407–446, doi:10.1080/07055900.1995.9649539.